Les Cahiers du GERAD ISSN: 0711–2440

Joint mixed-integer convex optimization of path, speed, and power in hybrid-electric ships

L-P. Baillargeon, M. Berger, A. Lesage-Landry

G–2026–52

September 2026

La publication de ces rapports de recherche est rendue possible grâce au soutien de HEC Montréal, Polytechnique Montréal, Université McGill, Université du Québec à Montréal, ainsi que du Fonds de recherche du Québec – Nature et technologies.

Dépôt légal – Bibliothèque et Archives nationales du Québec, 2026
– Bibliothèque et Archives Canada, 2026

The publication of these research reports is made possible thanks to the support of HEC Montréal, Polytechnique Montréal, McGill University, Université du Québec à Montréal, as well as the Fonds de recherche du Québec – Nature et technologies.

Legal deposit – Bibliothèque et Archives nationales du Québec, 2026
– Library and Archives Canada, 2026

GERAD HEC Montréal
3000, chemin de la Côte-Sainte-Catherine
Montréal (Québec) Canada H3T 2A7

Tél. : 514 340-6053
Téléc. : 514 340-5665
info@gerad.ca
www.gerad.ca

Joint mixed-integer convex optimization of path, speed, and power in hybrid-electric ships

Louis-Philippe Baillargeon [a, d, e]

Maxime Berger [b, c]

Antoine Lesage-Landry [a, c, d, e]

[a] *Polytechnique Montréal, Montréal (Qc), Canada, H3T 1J4*

[b] *Université de Sherbrooke, Sherbrooke (Qc), Canada, J1K 2R1*

[c] *Université du Québec à Rimouski, Rimouski (Qc), Canada, G5L3A1*

[d] *GERAD, Montréal (Qc), Canada, H3T 1J4*

[e] *LORER, Montréal (Qc), Canada, H3T 1J4*

louis-philippe.baillargeon@etud.polymtl.ca
Maxime.Berger@usherbrooke.ca
antoine.lesage-landry@polymtl.ca

September 2026
Les Cahiers du GERAD
G–2026–52

Abstract : We present optimization models that simultaneously determine ship path, speed profile, and hybrid power system operations. Our approach integrates solar photovoltaics, shore power, batteries, and diesel generators while accounting for power balance, propulsion physics, and itinerary constraints. To optimize path while avoiding obstacles, e.g., land, shallow waters, or protected areas, the nonconvex navigable space is partitioned into convex, obstacle-free sets, which can be embedded into the optimization problem using disjunctive constraints. The convex sets also serve to evaluate the impact of spatially varying environmental conditions, such as solar irradiance, wind, and currents on energy efficiency. Four models that balance the tradeoff between model accuracy and computational burden differently are formulated as mixed-integer convex programs (MICPs), solvable to global optimality using off-the-shelf commercial solvers. Four numerical case studies based on the S-175 ship model and historical ERA5 and Copernicus Marine data show that the models reduce operating costs relative to a shortest-path constant-speed baseline. In a synthetic case subject to brief adverse environmental conditions, modelling the coupling between passage time and environmental conditions enables the ship to delay its passage through the affected region and yields savings of up to 16.89%. In real-data cases, joint path optimization yields average savings of 14.22% when navigating Gulf of St. Lawrence seasonal speed restrictions and 5.92% when exploiting favourable environmental conditions. When the shortest path is already optimal, all optimization-based methods yield similar savings (≈1%), highlighting that the benefits of our models arise when environmental or operational conditions create opportunities for route adaptation.

Keywords: Mixed-integer convex programming; hybrid-electric ships; shipboard power systems; weather-routing; speed optimization

Résumé : Cet article propose un modèle d'optimisation pour planifier conjointement la trajectoire, le profil de vitesse et le réseau d'alimentation électrique d'un navire hybride-électrique. Le navire considéré comprend des génératrices diesel, une batterie, des panneaux photovoltaïques ainsi que l'infrastructure permettant l'alimentation électrique à quai. Le modèle prend en compte l'horaire du voyage, l'évitement des obstacles, les limites de vitesse, la résistance hydrodynamique, le système de propulsion et l'équilibre de puissance électrique. À notre connaissance, il s'agit du premier cadre d'optimisation convexe en nombres entiers mixtes permettant d'optimiser simultanément une trajectoire bidimensionnelle libre, la vitesse et la gestion énergétique d'un navire hybride-électrique. Le domaine navigable non convexe est décomposé en ensembles convexes sans obstacle. Des variables binaires déterminent l'ensemble convexe occupé par le navire à chaque instant et activent simultanément les valeurs des courants, des vents, de l'irradiance solaire et des limites de vitesse applicables à cet ensemble et à cet instant. Cette approche permet de prendre en compte les variations spatiotemporelles des conditions environnementales. Des approximations convexes de la résistance causée par la friction de l'eau et de l'air et de la puissance propulsive, permettent de formuler le problème comme un programme convexe en nombres entiers mixtes, qui peut être résolu jusqu'à l'optimalité globale par des logiciels comerciaux standards. Quatre formulations offrant différents compromis entre fidélité et temps de calcul sont évaluées avec le modèle de navire S-175 dans une étude de cas utilisant des données environnementales historiques. Dans le cas synthétique, la représentation spatiotemporelle permet d'éviter une perturbation locale et de réduire les coûts jusqu'à 16,89 %. Dans les cas réels où le plus court chemin est défavorable, l'optimisation conjointe de la trajectoire permet des économies moyennes atteignant 14,22 % en présence de zones de réduction de vitesse et 5,92 % à proximité du Gulf Stream. Lorsque le plus court chemin demeure favorable, les gains sont plus modestes et les formulations à trajectoire fixe offrent un meilleur compromis entre la qualité des solutions et le temps de calcul.

Mots clés : Optimisation convexe en nombres entiers mixtes; navires hybrides-électriques; systèmes électriques de bord; routage météorologique; optimisation de la vitesse

Acknowledgements: This work was supported by the Ministère de l'Économie, de l'Innovation et de l'Énergie (MEIE) of Québec and Canada Steamship Lines (CSL), through funding awarded to Innovation Maritime (IMAR) under the Programme de soutien aux organismes de recherche et d'innovation (PSO), Volet 2a – Soutien aux projets de recherche-innovation. The Fonds de recherche du Québec en Sciences et Technologies (FRQNT) also supported an internship at IMAR through its *Bourses de 2e cycle pour stage en Centre collégial de transfert de technologies* (CCTT) scholarship program. This internship helped ground our work in maritime operational realities. We thank Sébastien Duquette (Innovation Maritime) and Alain Richard (AREN Expert Nautique) for their valuable practical insights. Sponsors had no role in study design, data collection/analysis, writing, and the decision to submit.

During the preparation of this work, the authors used ChatGPT (OpenAI) to assist with language editing, including improving clarity, concision, and phrasing; all scientific content and conclusions are entirely the authors' own. The authors reviewed and edited all AI-assisted content and take full responsibility for the content of the published article.

1 Introduction

Maritime shipping is among the most greenhouse gas (GHG)-efficient freight modes per tonne-kilometre [1], yet nearly all cargo ships still rely primarily on fossil fuels [2]. Battery-electric propulsion can be economical on shorter routes, but full electrification of larger ships on longer voyages remains contingent on advances in battery technology and charging infrastructure [2, 3]. Diesel is expected to remain cheaper than carbon-neutral fuels until 2050 [4]. Hybrid-electric ships therefore offer a practical near-term pathway by combining diesel generation with batteries, solar power and shore electricity [2, 5, 6]. By shifting peak loads to batteries and using cleaner, cheaper shore electricity when available, these systems can reduce emissions and operating costs while retaining the range provided by onboard generation [6, 7]. The battery-equipped fleet has expanded rapidly: EMSA's 2023 report identifies more than 800 such ships in operation worldwide, over three times the number five years earlier [8]. Realizing these benefits, however, requires coordinating power system operation with vessel motion, as path, speed, and power system decisions strongly affect fuel consumption under spatially and temporally varying winds, currents, and solar irradiance [9].

Path planning, speed scheduling, and power system operation have each been studied separately [9–11]. The joint speed-power optimization problem has been formulated as a convex program [12], mixed-integer linear program (MILP) [13, 14], mixed-integer convex quadratic program (MICQP) [15], and mixed-integer nonlinear program (MINLP) [16, 17]. It has also been addressed through heuristic decompositions [18] and particle swarm optimization (PSO) [19]. Joint path-speed optimization has been studied using dynamic programming [20], graph-search methods based on Dijkstra [21], PSO [22], genetic algorithms [23], and reinforcement learning [24]. The aforementioned integrated approaches can outperform sequential optimization [9], but few studies coordinate all three decision layers. For instance, [25] optimizes speed and power while selecting among a finite set of precomputed paths. However, the candidate paths are generated independently of speed and power decisions, preventing both from influencing path generation and potentially excluding better solutions. To the best of our knowledge, only two studies jointly optimize free-path planning, speed, and power for hybrid-electric ships [26, 27], and neither offers a deterministic mixed-integer convex program (MICP) model that can be solved to global optimality with industrial solvers. Free-path ship routing is difficult to formulate as an MICP because obstacle avoidance makes the navigable domain nonconvex. The graph of convex sets (GCS) framework handles this geometry by decomposing free space into interconnected convex regions and using binary variables to select the region sequence [28]. Recent work extends GCS into space-time by augmenting convex sets with a continuous time coordinate, yielding time-optimal piecewise-linear robot trajectories with flexible arrival times and velocity bounds around dynamic obstacles [29]. This segment-based representation does not address the fixed-clock coupling required here among spatially and temporally varying environmental fields, scalar vessel speed, resistance, propulsion, and hybrid-power states under a prescribed itinerary. We therefore introduce a time-indexed spatial decomposition that supports these physical and operational couplings.

To address the limitations identified above, this work makes the following contributions:

- We develop a binary, time-indexed model in which convex-region variables enforce navigability and activate spatially and temporally varying environmental conditions and speed limits.
- We refine convex approximations of water resistance and propulsion power and propose the first convex approximation of Blendermann wind resistance for free-heading ship path planning.
- We formulate the first deterministic MICP model for jointly optimizing a continuous two-dimensional ship path, speed profile, and hybrid power system schedule under spatially and temporally varying environmental and regulatory conditions.
- We propose four optimization models: Joint Path-Speed-Power optimization with Continuous speed (`JoPSPo-C`), Joint Path-Speed-Power optimization with Discrete speed (`JoPSPo-D`), Fixed-Path joint Speed-Power optimization with Space-Time environment (`FiPSPo-ST`), and Fixed-

Path joint Speed-Power optimization with Trajectory-Indexed environment (`FiPSPo-TI`), which provide different trade-offs between modelling accuracy and computational complexity.

The remainder of this paper is organized as follows. Section 2 presents the proposed models, Section 3 describes the case studies and evaluation methodology, and Section 4 presents and discusses the numerical results.

2 Mixed-integer convex program models

This section develops four MICP models coupling navigation, spatio-temporal environmental conditions, resistance, propulsion, and hybrid-power operation. They share the navigation and power system constraints but differ in path representation and environmental coupling.

2.1 Navigation and environmental coupling

Let $n_\mathrm{t} \in \mathbb{N}$ denote the number of time intervals, each of duration $\delta > 0$. The ship position is represented by the decision variable $\mathbf{X} \in \mathbb{R}^{(n_\mathrm{t}+1)\times 2}$, whose t-th row $\mathbf{x}^t = (x^{t,0}, x^{t,1}) \in \mathbb{R}^2$ describes the eastward and northward distances from the origin at instant t. The sets of time instants and intervals are $\mathcal{T} = \{0, 1, \ldots, n_\mathrm{t}\}$, and $\mathcal{T}^\delta = \{0, 1, \ldots, n_\mathrm{t} - 1\}$, respectively, where interval $t \in \mathcal{T}^\delta$ extends from instant t to instant $t + 1$. Schedule requirements are enforced by fixing the ship position during each port call, indexed by $\mathcal{H} \subset \mathbb{N}$. Each port call $h \in \mathcal{H}$ is associated with coordinates $\mathbf{x}^h \in \mathbb{R}^2$ and a set of time instants $\mathcal{T}^h_\mathrm{port} \subseteq \mathcal{T}$. The set of time intervals during which the ship remains docked at a port is

$$\mathcal{T}^\delta_\mathrm{port} = \bigcup_{h\in\mathcal{H}} \left\{ t \in \mathcal{T}^\delta \;\middle|\; t, t+1 \in \mathcal{T}^h_\mathrm{port} \right\}.$$

Port stops are imposed as

$$\mathbf{x}^t = \mathbf{x}^h, \quad \forall h \in \mathcal{H},\ \forall t \in \mathcal{T}^h_\mathrm{port}. \tag{1}$$

Let $\underline{\mathbf{x}}, \overline{\mathbf{x}} \in \mathbb{R}^2$ denote the lower and upper coordinate bounds of the considered region. The ship position satisfies

$$\underline{\mathbf{x}} \le \mathbf{x}^t \le \overline{\mathbf{x}}, \quad \forall t \in \mathcal{T}. \tag{2}$$

The nonconvex navigable region is decomposed into $n_\mathrm{s} \in \mathbb{N}$ obstacle-free convex sets, indexed by $\mathcal{S} = \{0, 1, \ldots, n_\mathrm{s} - 1\}$. This decomposition restricts the searchable navigable space because covering the entire feasible region with convex sets is generally impractical. Adjacent convex sets are constructed from shared boundary vertices such that their interiors are disjoint and their intersection is limited to a common edge. Consequently, any point constrained to belong to both sets lies on their shared boundary. We introduce binary set-selection variables $\mathbf{Z} \in \{0, 1\}^{n_\mathrm{s}\times(n_\mathrm{t}+1)}$, where $Z^{s,t} = 1$ indicates that the ship occupies convex set s at time instant t. The ship is constrained to occupy exactly one convex set at a time:

$$\sum_{s=0}^{n_\mathrm{s}-1} Z^{s,t} = 1, \quad \forall t \in \mathcal{T}. \tag{3}$$

The variable $Z^{s,t}$ determines the convex set membership. Each set is characterized by $n_\mathrm{j} \in \mathbb{N}$ linear inequalities with coefficients $\mathbf{\Lambda}_1, \mathbf{\Lambda}_2, \mathbf{\Lambda}_3 \in \mathbb{R}^{n_\mathrm{j}\times n_\mathrm{s}}$:

$$\Lambda_1^{j,s} X^{t,1} + \Lambda_2^{j,s} X^{t,0} + \Lambda_3^{j,s} \ge -M^{j,s}_\mathrm{pos}(1 - Z^{s,t}), \quad \forall t \in \mathcal{T}, j \in \{0, 1, \ldots, n_\mathrm{j} - 1\}, s \in \mathcal{S}. \tag{4}$$

The position bounds in (2) enable explicit computation of tight big-M constants $M^{j,s}_\mathrm{pos} \in \mathbb{R}_+$ for each convex set inequality, improving solver performance. The same binary variables $Z^{s,t}$ are also used to model experienced environmental conditions. Let $\mathbf{C} \in \mathbb{R}^{n_\mathrm{s} \times n_\mathrm{t} \times 2}$, $\mathbf{W} \in \mathbb{R}^{n_\mathrm{s} \times n_\mathrm{t} \times 2}$, and $\mathbf{I} \in \mathbb{R}_+^{n_\mathrm{s} \times n_\mathrm{t}}$ contain the average current velocity, wind velocity, and solar irradiance in each convex set and time interval, respectively. For each $s \in \mathcal{S}$ and $t \in \mathcal{T}^\delta$, let $\mathbf{c}^{s,t} = [C^{s,t,0},\, C^{s,t,1}]^\top \in \mathbb{R}^2$ denote the current-velocity vector associated with convex set s during time interval t. Currents experienced by the ship at the beginning and end of each time interval, $\mathbf{c}_1^t, \mathbf{c}_2^t \in \mathbb{R}^2$, are computed as

$$\mathbf{c}_1^t = \sum_{s=0}^{n_\mathrm{s}-1} \mathbf{c}^{s,t} Z^{s,t}, \quad \mathbf{c}_2^t = \sum_{s=0}^{n_\mathrm{s}-1} \mathbf{c}^{s,t} Z^{s,t+1}, \quad \forall t \in \mathcal{T}^\delta. \tag{5}$$

We denote the solar irradiance experienced at the beginning and end of each time interval by $\mathbf{i}_1, \mathbf{i}_2 \in \mathbb{R}_+^{n_\mathrm{t}}$ and express these quantities as:

$$i_1^t = \sum_{s=0}^{n_\mathrm{s}-1} I^{s,t} Z^{s,t}, \quad i_2^t = \sum_{s=0}^{n_\mathrm{s}-1} I^{s,t} Z^{s,t+1}, \quad \forall t \in \mathcal{T}^\delta. \tag{6}$$

This set-activation structure is similar to that of [30]. To our knowledge, this is its first use in an MICP for ship voyage planning. The ship speed is bounded by its own maximum operating speed $\overline{v}$:

$$\hat{v}^t \leq \overline{v}, \quad \forall t \in \mathcal{T}^\delta. \tag{7}$$

To incorporate space-time varying speed limits, we define the speed limit matrix $\overline{\mathbf{V}} \in \mathbb{R}_+^{n_\mathrm{s} \times n_\mathrm{t}}$ and apply it to both endpoints of each time interval:

$$\hat{v}^t \leq \sum_{s=0}^{n_\mathrm{s}-1} \overline{V}^{s,t} Z^{s,t}, \quad \hat{v}^t \leq \sum_{s=0}^{n_\mathrm{s}-1} \overline{V}^{s,t} Z^{s,t+1}, \quad \forall t \in \mathcal{T}^\delta. \tag{8}$$

Minimum-speed constraints are omitted because lower bounds on velocity norms are nonconvex in the free-path models. At ports, the ship is required to remain stationary:

$$\hat{v}^t = 0, \quad \forall t \in \mathcal{T}^\delta_{\mathrm{port}}. \tag{9}$$

Let $\mathbf{A} \in \{0,1\}^{n_\mathrm{s} \times n_\mathrm{s}}$ denote the adjacency matrix of the convex set graph, where $A^{s,s'} = 1$ if a transition from set s to set s' is allowed. Let $\mathcal{A}_0 = \{(s,s') \in \mathcal{S} \times \mathcal{S} \mid A^{s,s'} = 0\}$ denote the set of forbidden transitions. Transitions between non-adjacent sets are restricted by imposing

$$Z^{s,t} + Z^{s',t+1} \leq 1, \quad \forall t \in \mathcal{T}^\delta,\ \forall (s,s') \in \mathcal{A}_0. \tag{10}$$

This restriction is consistent with our environmental model, which can represent occupancy of at most two sets during an interval. The interval duration δ should be sufficiently short that travelling across more than one set boundary within an interval is either physically impossible or never optimal.

2.2 Path modes

Constraints (3) and (4) ensure that each discrete-time position $\mathbf{x}^t$ lies in a convex set, but not that the trajectory between $\mathbf{x}^t$ and $\mathbf{x}^{t+1}$ remains navigable. We address this through four models with different trade-offs: joint path-speed-power, continuous speed optimization (`JoPSPo-C`), joint path-speed-power, discrete speed optimization (`JoPSPo-D`), fixed-path speed-power optimization, space-time environment (`FiPSPo-ST`), and fixed-path speed-power optimization, trajectory-indexed environment (`FiPSPo-TI`).

2.2.1 Joint path-speed-power optimization, continuous-speed

For each time interval t, we introduce a helper point $\mathbf{q}^t \in \mathbb{R}^2$, collected in $\mathbf{Q} \in \mathbb{R}^{n_\mathrm{t} \times 2}$, and bound it in the considered region:

$$\underline{\mathbf{x}} \leq \mathbf{q}^t \leq \overline{\mathbf{x}}, \quad \forall t \in \mathcal{T}^\delta. \tag{11}$$

Helper points lie in both convex sets occupied at time instants t and $t+1$:

$$\Lambda_1^{j,s} Q^{t,1} + \Lambda_2^{j,s} Q^{t,0} + \Lambda_3^{j,s} \geq -M_{\mathrm{q}}^{j,s}(1 - Z^{s,t}),\ \Lambda_1^{j,s} Q^{t,1} + \Lambda_2^{j,s} Q^{t,0} + \Lambda_3^{j,s} \geq -M_{\mathrm{q}}^{j,s}(1 - Z^{s,t+1}), \quad (12)$$

for all $t \in \mathcal{T}^\delta$, $j \in \{0, 1, \ldots, n_\mathrm{j} - 1\}$, and $s \in \mathcal{S}$. Big-M constant $M_\mathrm{q}^{j,s}$ can be computed tightly from (11). During a transition, $\mathbf{q}^t$ lies on the boundary shared by the two active convex sets. The nonnegative length variables $\boldsymbol{\ell}_1, \boldsymbol{\ell}_2 \in \mathbb{R}_+^{n_\mathrm{t}}$ satisfy:

$$\ell_1^t = \left\| \mathbf{q}^t - \mathbf{x}^t \right\|_2, \quad \ell_2^t = \left\| \mathbf{x}^{t+1} - \mathbf{q}^t \right\|_2 \quad \forall t \in \mathcal{T}^\delta. \quad (13)$$

The following convex relaxation of (13) is exact because travelled distance is minimized implicitly through the objective of Section 2.4 and propulsion constraints of Section 2.3.

$$\ell_1^t \geq \left\| \mathbf{q}^t - \mathbf{x}^t \right\|_2, \quad \ell_2^t \geq \left\| \mathbf{x}^{t+1} - \mathbf{q}^t \right\|_2, \quad \forall t \in \mathcal{T}^\delta. \quad (14)$$

Assuming negligible acceleration time, speed magnitude $\hat{\mathbf{v}} \in \mathbb{R}_+^{n_\mathrm{t}}$ is

$$\hat{v}^t = \frac{\ell_1^t + \ell_2^t}{\delta}, \quad \forall t \in \mathcal{T}^\delta. \quad (15)$$

Under this constant-speed command, the corresponding leg durations for sailing intervals $\boldsymbol{\delta}_1, \boldsymbol{\delta}_2 \in \mathbb{R}_+^{n_\mathrm{t}}$ and directional velocities $\mathbf{v}_1^t, \mathbf{v}_2^t \in \mathbb{R}^2$ are

$$\delta_1^t = \delta \frac{\ell_1^t}{\ell_1^t + \ell_2^t}, \quad \delta_2^t = \delta \frac{\ell_2^t}{\ell_1^t + \ell_2^t}, \quad \mathbf{v}_1^t = \frac{\mathbf{q}^t - \mathbf{x}^t}{\delta_1^t}, \quad \mathbf{v}_2^t = \frac{\mathbf{x}^{t+1} - \mathbf{q}^t}{\delta_2^t}, \quad \forall t \in \mathcal{T}^\delta.$$

These exact directional velocities cannot be represented using convex constraints. Thus, directional speed matrix $\mathbf{V} \in \mathbb{R}^{n_\mathrm{t} \times 2}$ with rows $\mathbf{v}^t \in \mathbb{R}^2$ is approximated using the average velocity over the full time interval:

$$\mathbf{v}^t = \frac{\mathbf{x}^{t+1} - \mathbf{x}^t}{\delta}, \quad \forall t \in \mathcal{T}^\delta. \quad (16)$$

When the ship remains in a convex set, (16) is exact: constant environmental conditions make any deviation from the segment joining $\mathbf{x}^t$ and $\mathbf{x}^{t+1}$ increase distance, speed, propulsion power, and cost without benefit. Thus, $\mathbf{q}^t$ lies on this segment and both leg velocities equal the interval-average velocity. During a set transition, the segment may leave the selected sets or differing conditions may favour distinct headings, causing $\mathbf{q}^t$ to deviate and (16) to become approximate. Let $\boldsymbol{\ell}_{\mathrm{w}1}, \boldsymbol{\ell}_{\mathrm{w}2} \in \mathbb{R}_+^{n_\mathrm{t}}$ denote the water-relative distances travelled on the first and second legs, respectively. The current contribution on each leg is computed assuming equal leg durations $\boldsymbol{\delta}_1 = \boldsymbol{\delta}_2 = \delta/2$, even if by design, leg durations are not necessarily equal,

$$\ell_{\mathrm{w}1}^t \geq \left\| \mathbf{q}^t - \mathbf{x}^t - \frac{\delta}{2} \mathbf{c}_1^t \right\|_2, \quad \ell_{\mathrm{w}2}^t \geq \left\| \mathbf{x}^{t+1} - \mathbf{q}^t - \frac{\delta}{2} \mathbf{c}_2^t \right\|_2, \quad \forall t \in \mathcal{T}^\delta. \quad (17)$$

These inequalities are tight at optimality because overestimating water-relative speed can only increase cost. The interval water-relative speed magnitude is then computed as

$$\hat{v}_\mathrm{w}^t = \frac{\ell_{\mathrm{w}1}^t + \ell_{\mathrm{w}2}^t}{\delta}, \quad \forall t \in \mathcal{T}^\delta. \quad (18)$$

Experienced solar irradiance during the full time interval $\mathbf{i} \in \mathbb{R}_+^{n_\mathrm{t}}$ is also approximated with the average assuming equal time spent in each sets, leading to

$$\mathbf{i} = \frac{\mathbf{i}_1 + \mathbf{i}_2}{2}. \quad (19)$$

2.2.2 Joint path-speed-power optimization, discrete-speed

Unlike `JoPSPo-C`, `JoPSPo-D` fixes transitions at interval midpoints, giving each leg duration $\delta/2$ and allowing its ground- and water-relative velocity vectors to be computed exactly with convex constraints. Treating transition points as path states also allows speed and power to adapt independently on each leg. The path is therefore represented by $\mathbf{X} \in \mathbb{R}^{(2n_\mathrm{t}+1)\times 2}$, with rows $\mathbf{x}^t \in \mathbb{R}^2$. Even-indexed positions $\mathbf{x}^{2t}$ correspond to the original instants $t \in \{0, 1, \ldots, n_\mathrm{t}\}$, whereas odd-indexed positions $\mathbf{x}^{2t+1}$ represent interval midpoints for $t \in \{0, 1, \ldots, n_\mathrm{t} - 1\}$. The set-selection variables are unchanged: $Z^{s,t} = 1$ identifies the set occupied at original instant t. Each even-indexed position must belong to its selected set:

$$\Lambda_1^{j,s} X^{2t,1} + \Lambda_2^{j,s} X^{2t,0} + \Lambda_3^{j,s} \geq -M_\mathrm{pos}^{j,s}(1 - Z^{s,t}), \quad \forall t \in \mathcal{T}, j \in \{0, 1, \ldots, n_\mathrm{j} - 1\}, s \in \mathcal{S}. \tag{20}$$

Each odd-indexed position must belong to both sets selected at the adjacent original instants:

$$\Lambda_1^{j,s} X^{2t+1,1} + \Lambda_2^{j,s} X^{2t+1,0} + \Lambda_3^{j,s} \geq -M_\mathrm{pos}^{j,s}(1 - Z^{s,t}), \tag{21}$$
$$\Lambda_1^{j,s} X^{2t+1,1} + \Lambda_2^{j,s} X^{2t+1,0} + \Lambda_3^{j,s} \geq -M_\mathrm{pos}^{j,s}(1 - Z^{s,t+1}), \tag{22}$$

for all $t \in \mathcal{T}^\delta$, $j \in \{0, 1, \ldots, n_\mathrm{j} - 1\}$, and $s \in \mathcal{S}$. Ship speed matrix $\mathbf{V} \in \mathbb{R}^{2n_\mathrm{t}\times 2}$ with rows $\mathbf{v}^t \in \mathbb{R}^2$ is computed on each half time interval independently using:

$$\mathbf{v}^t = 2\frac{\mathbf{x}^{t+1} - \mathbf{x}^t}{\delta}, \quad \forall t \in \{0, 1, \ldots, 2n_\mathrm{t} - 1\}, \tag{23}$$
$$\hat{v}^t = \|\mathbf{v}^t\|_2, \quad \forall t \in \{0, 1, \ldots, 2n_\mathrm{t} - 1\}. \tag{24}$$

Equation (23) is affine. Although the equality in (24) is nonconvex, it admits the following exact second-order cone convex relaxation because speed is minimized through the propulsion constraints and objective:

$$\hat{v}^t \geq \|\mathbf{v}^t\|_2, \quad \forall t \in \{0, 1, \ldots, 2n_\mathrm{t} - 1\}. \tag{25}$$

Water-relative speed matrix $\mathbf{V}_\mathrm{w} \in \mathbb{R}^{2n_\mathrm{t}\times 2}$ with rows $\mathbf{v}_\mathrm{w}^t \in \mathbb{R}^2$ is then expressed as

$$\mathbf{v}_\mathrm{w}^{2t} = \mathbf{v}^{2t} - \mathbf{c}_1^t, \quad \mathbf{v}_\mathrm{w}^{2t+1} = \mathbf{v}^{2t+1} - \mathbf{c}_2^t \quad \forall t \in \mathcal{T}^\delta. \tag{26}$$

Water-relative speed magnitude $\hat{\mathbf{v}}_\mathrm{w} \in \mathbb{R}_+^{2n_\mathrm{t}}$ is defined by

$$\hat{v}_\mathrm{w}^t = \left\|\mathbf{v}_\mathrm{w}^t\right\|_2 \quad \forall t \in \{0, 1, \ldots, 2n_\mathrm{t} - 1\}. \tag{27}$$

We replace (27) with the following exact second-order cone relaxation:

$$\hat{v}_\mathrm{w}^t \geq \left\|\mathbf{v}_\mathrm{w}^t\right\|_2 \quad \forall t \in \{0, 1, \ldots, 2n_\mathrm{t} - 1\}. \tag{28}$$

The solar irradiance computed in (6) can be applied independently on even and odd time intervals. `JoPSPo-D`'s main limitation is that convex set transitions occur only at half-time step instants, discretizing admissible transition times and potentially restricting representable path–speed profiles, especially for large δ. Reducing δ refines this grid but increases computational burden.

2.2.3 Fixed-path speed-power optimization, space-time environment

`FiPSPo-ST` uses a parameterized fixed path while retaining the space-time environmental model. It represents ship position by the scalar path coordinate d^t, collected in $\mathbf{d} \in \mathbb{R}_+^{n_\mathrm{t}+1}$. The port constraints in (1) are reformulated by fixing d^t to the cumulative path distance d^h of port h:

$$d^t = d^h \quad \forall h \in \mathcal{H},\ \forall t \in \mathcal{T}_\mathrm{port}^h. \tag{29}$$

Considered region bounds (2) reduce to:

$$\underline{d} \leq d^t \leq \overline{d}, \quad \forall t \in \mathcal{T}, \tag{30}$$

where $\underline{d}$ and $\overline{d}$ denote the initial and terminal cumulative path distances, respectively. In `FiPSPo-ST`, convex sets represent consecutive fixed-path segments, and $Z^{s,t}$ identifies the segment occupied at instant t. Let $\bar{d}^s$ and $\bar{d}^{s+1}$ denote the initial and terminal cumulative distances of segment s. The membership constraint (4) becomes:

$$d^t \geq \sum_{s=0}^{n_{\mathrm{s}}-1} \bar{d}^s Z^{s,t}, \quad d^t \leq \sum_{s=0}^{n_{\mathrm{s}}-1} \bar{d}^{s+1} Z^{s,t}, \quad \forall t \in \mathcal{T}, \tag{31}$$

and speed magnitude becomes:

$$\hat{v}^t = \frac{d^{t+1} - d^t}{\delta} \quad \forall t \in \mathcal{T}^\delta. \tag{32}$$

Directional speed vectors can be represented exactly using the known heading of each segment θ^s. We introduce the auxiliary variables $\mathbf{U}_1 \in \mathbb{R}_+^{n_{\mathrm{s}} \times n_{\mathrm{t}}}$ and $\mathbf{U}_2 \in \mathbb{R}_+^{n_{\mathrm{s}} \times n_{\mathrm{t}}}$, which disaggregate the speed magnitude:

$$\sum_{s=0}^{n_{\mathrm{s}}-1} U_1^{s,t} = \hat{v}^t, \qquad \sum_{s=0}^{n_{\mathrm{s}}-1} U_2^{s,t} = \hat{v}^t, \quad \forall t \in \mathcal{T}^\delta, \tag{33}$$

$$U_1^{s,t} \leq \overline{v} Z^{s,t}, \qquad U_2^{s,t} \leq \overline{v} Z^{s,t+1}, \quad \forall t \in \mathcal{T}^\delta,\ \forall s \in \mathcal{S}. \tag{34}$$

The directional speed vectors associated with the beginning and end of each time interval $\mathbf{v}_1^t, \mathbf{v}_2^t \in \mathbb{R}^2$, respectively, are then given exactly by

$$v_1^{t,0} = \sum_{s=0}^{n_{\mathrm{s}}-1} U_1^{s,t} \cos(\theta^s), \qquad v_1^{t,1} = \sum_{s=0}^{n_{\mathrm{s}}-1} U_1^{s,t} \sin(\theta^s), \quad \forall t \in \mathcal{T}^\delta, \tag{35}$$

$$v_2^{t,0} = \sum_{s=0}^{n_{\mathrm{s}}-1} U_2^{s,t} \cos(\theta^s), \qquad v_2^{t,1} = \sum_{s=0}^{n_{\mathrm{s}}-1} U_2^{s,t} \sin(\theta^s), \quad \forall t \in \mathcal{T}^\delta. \tag{36}$$

The start and end water-relative velocity vectors $\mathbf{v}_{\mathrm{w}1}^t, \mathbf{v}_{\mathrm{w}2}^t \in \mathbb{R}^2$ are:

$$\mathbf{v}_{\mathrm{w}1}^t = \mathbf{v}_1^t - \mathbf{c}_1^t, \quad \mathbf{v}_{\mathrm{w}2}^t = \mathbf{v}_2^t - \mathbf{c}_2^t, \quad \forall t \in \mathcal{T}^\delta. \tag{37}$$

The corresponding water-relative speed magnitudes $\hat{\mathbf{v}}_{\mathrm{w}1}, \hat{\mathbf{v}}_{\mathrm{w}2} \in \mathbb{R}_+^{n_{\mathrm{t}}}$ are computed through exact second-order cone relaxations:

$$\hat{v}_{\mathrm{w}1}^t \geq \left\|\mathbf{v}_{\mathrm{w}1}^t\right\|_2, \quad \hat{v}_{\mathrm{w}2}^t \geq \left\|\mathbf{v}_{\mathrm{w}2}^t\right\|_2, \quad \forall t \in \mathcal{T}^\delta. \tag{38}$$

Unlike in `JoPSPo-D`, the endpoint magnitudes in (38) cannot define leg-specific resistance and power decisions because weighting energy and cost by variable leg durations would introduce nonconvex products in the battery state-of-charge and cost equations unless we fix transition times. The interval water-relative speed magnitude is therefore approximated by their mean:

$$\hat{v}_{\mathrm{w}}^t = \frac{\hat{v}_{\mathrm{w}1}^t + \hat{v}_{\mathrm{w}2}^t}{2}, \quad \forall t \in \mathcal{T}^\delta. \tag{39}$$

The solar irradiance also needs to be averaged over each time interval as in (19).

2.2.4 Fixed-path speed-power optimization, trajectory-indexed environment

`FiPSPo-TI` applies the space-time interpolation strategy of [31] to the hybrid-ship joint speed-power problem. Unlike the distance-indexed mode in [31], it is time-indexed and uses the port constraints, bounds, and speed definition as (29), (30), and (32), respectively. Ship position is estimated from a reference trajectory with cumulative-distance profile $\tilde{\mathbf{d}} \in \mathbb{R}_+^{n_t+1}$. Let $\mathbf{x}_{\text{path}}(d) \in \mathbb{R}^2$ map cumulative path distance d to geographical coordinates. Reference position during interval t is approximated by

$$\tilde{\mathbf{x}}^t = \mathbf{x}_{\text{path}} \left(\frac{\tilde{d}^t + \tilde{d}^{t+1}}{2} \right), \qquad \forall t \in \mathcal{T}^\delta. \tag{40}$$

Ship heading is likewise precomputed from

$$\tilde{\theta}^t = \theta_{\text{path}} \left(\frac{\tilde{d}^t + \tilde{d}^{t+1}}{2} \right), \qquad \forall t \in \mathcal{T}^\delta, \tag{41}$$

where $\theta_{\text{path}}(d)$ denotes the fixed-path heading at d. Rather than using the set-based definitions (5)–(6), the environmental fields are linearly interpolated at reference midpoint $\tilde{\mathbf{x}}^t$ and mid-interval time from surrounding spatial grid points and adjacent forecast times. This yields experienced current $\tilde{\mathbf{c}}^t$ and solar irradiance $\tilde{i}^t$, treated as fixed parameters during each solve:

$$\mathbf{c}^t = \tilde{\mathbf{c}}^t, \quad i^t = \tilde{i}^t, \quad \forall t \in \mathcal{T}^\delta. \tag{42}$$

Directional ground-speed vector is given by

$$\mathbf{v}^t = \hat{v}^t \begin{bmatrix} \cos\left(\tilde{\theta}^t\right) \\ \sin\left(\tilde{\theta}^t\right) \end{bmatrix}, \qquad \forall t \in \mathcal{T}^\delta. \tag{43}$$

Water-relative speed vector is then:

$$\mathbf{v}_{\text{w}}^t = \mathbf{v}^t - \mathbf{c}^t, \quad \forall t \in \mathcal{T}^\delta, \tag{44}$$

from which we can compute water-relative speed magnitude:

$$\hat{v}_{\text{w}}^t = \left\| \mathbf{v}_{\text{w}}^t \right\|_2, \quad \forall t \in \mathcal{T}^\delta, \tag{45}$$

with, again, the exact second-order cone relaxation at optimality:

$$\hat{v}_{\text{w}}^t \geq \left\| \mathbf{v}_{\text{w}}^t \right\|_2, \quad \forall t \in \mathcal{T}^\delta. \tag{46}$$

Because environmental parameters are fixed during each solve, they do not respond directly to changes in the optimized distance profile. After each solve, the reference distance, position, heading, and environmental profiles are updated from the optimized trajectory, and the problem is re-solved for a prescribed number of iterations.

2.2.5 Notation simplification

`JoPSPo-D` retains the original-time indexing for the convex set variables, adjacency constraints, and environmental forecast data, but divides each original interval into two half-intervals for motion, resistance, propulsion, and power system variables. Constraints imposed at original position instants apply to the even-indexed positions $\mathbf{x}^{2t}$, while position bounds apply to all $2n_{\text{t}} + 1$ original and mid-point positions. Both half-intervals within original interval t use environmental data from the same original forecast interval. Currents, solar irradiance, wind-resistance coefficients, and spatial speed limits associated with $Z^{s,t}$ apply to the first half-interval, whereas those associated with $Z^{s,t+1}$ apply to the second. All remaining interval-indexed variables and constraints are applied independently to both half-intervals, with original interval parameters, such as auxiliary load, shore-power availability, and electricity prices, repeated on both. Port speed and propulsion constraints likewise apply to both halves of each port interval. Battery dynamics are applied twice per original interval using a duration of $\delta/2$, with stored-energy bounds imposed at both original and midpoint states and the terminal condition imposed after the final half-interval. The objective is evaluated over the $2n_{\mathrm{t}}$ half-intervals using a duration of $\delta/2$, with original interval prices repeated on the corresponding two halves. To avoid duplicating the common models, the remainder of the paper uses the same interval index t for the original intervals of the other modes and the half-intervals of `JoPSPo-D`.

2.3 Resistance and propulsion models

The total ship resistance $\mathbf{r}_{\mathrm{tot}} \in \mathbb{R}_+^{n_{\mathrm{t}}}$ comprises calm-water resistance $\mathbf{r}_{\mathrm{cw}} \in \mathbb{R}_+^{n_{\mathrm{t}}}$ and wind resistance $\mathbf{r}_{\mathrm{wind}} \in \mathbb{R}^{n_{\mathrm{t}}}$. Wind resistance may reduce required thrust but cannot provide braking or generated power. Total resistance is imposed as the nonnegative epigraph constraint:

$$r_{\mathrm{tot}}^t \geq r_{\mathrm{cw}}^t + r_{\mathrm{wind}}^t, \quad r_{\mathrm{tot}}^t \geq 0, \quad \forall t \in \mathcal{T}^\delta. \tag{47}$$

At optimality, this relaxation recovers $r_{\mathrm{tot}}^t = \max\{r_{\mathrm{cw}}^t + r_{\mathrm{wind}}^t, 0\}$, because larger resistance only increases required thrust and operating cost. The model does not represent cases in which a following wind alone would accelerate the ship beyond its speed limit; such cases are assumed not to occur.

2.3.1 Fit range

The resistance and propulsion models use convex surrogates for nonlinear relationships from [32–34]. The nonlinear models are sampled offline over relevant decision variable ranges, and polynomial surrogates of up to fourth order are fitted to minimize squared error. Coefficients of second- to fourth-order terms are constrained to be nonnegative to impose convexity, as are linear speed magnitude and thrust coefficients, ensuring monotonicity and tight epigraph relaxations. The calm-water surrogate is fitted over the full admissible range, whereas the wind-resistance and propulsion surrogates require narrower, problem-specific ranges. These ranges are estimated from the shortest-path constant-speed (`SPaCS`) solution later introduced in Section 3.3, using scaled bounds on ship speed, total resistance, and propulsion power to balance fitting accuracy and extrapolation risk. The fitting-domain scale factors and fit quality are reported in A.

2.3.2 Calm-water resistance

A standard calm-water resistance model is the Molland model [32] :

$$r_{\mathrm{cw}}^t = \frac{1}{2}\rho_{\mathrm{w}} a_{\mathrm{wet}}^t c_{\mathrm{d}}(\hat{v}_{\mathrm{w}}^t) \left(\hat{v}_{\mathrm{w}}^t\right)^2, \quad \forall t \in \mathcal{T}^\delta, \tag{48}$$

where $\mathbf{a}_{\mathrm{wet}} \in \mathbb{R}_+^{n_{\mathrm{t}}}$ is the wetted surface area, $\rho_{\mathrm{w}} \in \mathbb{R}_+$ denotes the water density, and $c_{\mathrm{d}}(\hat{v}_{\mathrm{w}}^t)$ is a speed-dependent drag coefficient. The convex surrogate is expressed in terms of the normalized water-relative speed magnitude $\tilde{v}_{\mathrm{w}}^t = \hat{v}_{\mathrm{w}}^t/\overline{v} \in \mathbb{R}_+$, which improves numerical conditioning. Let $\boldsymbol{\beta}_{\mathrm{cw}} \in \mathbb{R}^5$ denote the fitted coefficients. Because excess resistance cannot reduce propulsion power or operating cost, the surrogate-based constraints take the form of the following inequality, which is tight at optimality:

$$r_{\mathrm{cw}}^t \geq \beta_{\mathrm{cw}}^0 + \beta_{\mathrm{cw}}^1 \tilde{v}_{\mathrm{w}}^t + \beta_{\mathrm{cw}}^2 \left(\tilde{v}_{\mathrm{w}}^t\right)^2 + \beta_{\mathrm{cw}}^3 \left(\tilde{v}_{\mathrm{w}}^t\right)^3 + \beta_{\mathrm{cw}}^4 \left(\tilde{v}_{\mathrm{w}}^t\right)^4, \quad \forall t \in \mathcal{T}^\delta. \tag{49}$$

2.3.3 Wind resistance

Wind resistance is computed using the nonconvex Blendermann model [33]. To our knowledge, this is the first convex approximation of the Blendermann model designed for free-heading ship path planning. A surrogate based only on air-relative speed magnitude performs poorly because wind may exceed ship speed and produce negative resistance. Directly including heading or angle of attack would introduce nonconvex trigonometric terms, so heading information is instead captured through the directional speed vector and magnitude. For each set-time pair, the wind vector is fixed and the Blendermann model is sampled over a narrow range of feasible ship speed vectors. Least-squares fitting then yields convex polynomial coefficients $\boldsymbol{\beta}^{s,t}_{\text{wind}} \in \mathbb{R}^{11}$, incorporated through disjunctive constraints:

$$\begin{aligned} r^t_{\text{wind}} \geq{}& \beta^{s,t,0}_{\text{wind}} + \beta^{s,t,1}_{\text{wind}}\tilde{v}^t + \beta^{s,t,2}_{\text{wind}}\left(\tilde{v}^t\right)^2 + \beta^{s,t,3}_{\text{wind}}\left(\tilde{v}^t\right)^3 + \beta^{s,t,4}_{\text{wind}}\left(\tilde{v}^t\right)^4 + \beta^{s,t,5}_{\text{wind}}\tilde{v}^{t,0} + \beta^{s,t,6}_{\text{wind}}\left(\tilde{v}^{t,0}\right)^2 \\ &+ \beta^{s,t,7}_{\text{wind}}\left(\tilde{v}^{t,0}\right)^4 + \beta^{s,t,8}_{\text{wind}}\tilde{v}^{t,1} + \beta^{s,t,9}_{\text{wind}}\left(\tilde{v}^{t,1}\right)^2 + \beta^{s,t,10}_{\text{wind}}\left(\tilde{v}^{t,1}\right)^4 - M_{\text{wind}}(1 - Z^{s,t}), \quad \forall s \in \mathcal{S},\ \forall t \in \mathcal{T}^\delta, \end{aligned} \tag{50}$$

where $\tilde{v}^t = \hat{v}^t/\overline{v}$, $\tilde{v}^{t,0} = v^{t,0}/\overline{v}$, and $\tilde{v}^{t,1} = v^{t,1}/\overline{v}$. Tight constants $M_{\text{wind}} \in \mathbb{R}_+$ are computed from the surrogate extrema over the feasible operating range. For ordered two-dimensional set decompositions, such as in Case # 2 described in Section 3.1, the fitting domain is restricted to a 90° range aligned with the direction required to cross each set, reducing fitting error. Because `FiPSPo-ST` uses a fixed path, each set heading is known, reducing the surrogate to a function of speed magnitude with coefficients $\boldsymbol{\beta}^{s,t}_{\text{wind}} \in \mathbb{R}^5$:

$$r^t_{\text{wind}} \geq \beta^{s,t,0}_{\text{wind}} + \beta^{s,t,1}_{\text{wind}}\tilde{v}^t + \beta^{s,t,2}_{\text{wind}}\left(\tilde{v}^t\right)^2 + \beta^{s,t,3}_{\text{wind}}\left(\tilde{v}^t\right)^3 + \beta^{s,t,4}_{\text{wind}}\left(\tilde{v}^t\right)^4 - M_{\text{wind}}(1 - Z^{s,t}), \quad \forall s \in \mathcal{S}, t \in \mathcal{T}^\delta. \tag{51}$$

For `FiPSPo-TI`, the same one-dimensional surrogate is fitted at each time step using the reference-trajectory environmental conditions from Section 2.2.4, without binary variables:

$$r^t_{\text{wind}} \geq \beta^{t,0}_{\text{wind}} + \beta^{t,1}_{\text{wind}}\tilde{v}^t + \beta^{t,2}_{\text{wind}}\left(\tilde{v}^t\right)^2 + \beta^{t,3}_{\text{wind}}\left(\tilde{v}^t\right)^3 + \beta^{t,4}_{\text{wind}}\left(\tilde{v}^t\right)^4, \quad \forall t \in \mathcal{T}^\delta. \tag{52}$$

2.3.4 Propulsion power

Propulsion power is modelled using the physics-based Wageningen B-series characteristics [34]. The propeller advance speed $\mathbf{u}_{\text{a}} \in \mathbb{R}^{n_{\text{t}}}_+$ is approximated using a constant wake fraction $w_{\text{f}} \in [0, 1]$:

$$u^t_{\text{a}} = \hat{v}^t_{\text{w}}(1 - w_{\text{f}}) \quad \forall t \in \mathcal{T}^\delta. \tag{53}$$

The nonconvex relationship among advance speed, rotational speed, thrust, and shaft power is approximated by a convex surrogate that captures propeller-efficiency variations across the operating range. For each sampled advance-speed and thrust pair, the required rotational speed and corresponding shaft power are computed. The surrogate is then embedded through the following relaxation, which is exact at optimality because overestimating propulsion power cannot improve the objective:

$$P^{p,t}_{\text{prop}} \geq \beta^{p,0}_{\text{prop}} + \beta^{p,1}_{\text{prop}}F^{p,t}_{\text{prop}} + \beta^{p,2}_{\text{prop}}(F^{p,t}_{\text{prop}})^2 + \beta^{p,3}_{\text{prop}}(F^{p,t}_{\text{prop}})^3 + \beta^{p,4}_{\text{prop}}u^t_{\text{a}} + \beta^{p,5}_{\text{prop}}(u^t_{\text{a}})^2 + \beta^{p,6}_{\text{prop}}(u^t_{\text{a}})^3, \tag{54}$$

for all $p \in \{0, 1, \ldots, n_{\text{p}} - 1\}$ and $t \in \mathcal{T}^\delta \setminus \mathcal{T}^\delta_{\text{port}}$, where n_{p} is the number of propellers, $\boldsymbol{\beta}^p_{\text{prop}} \in \mathbb{R}^7$ contains the fitted coefficients for propeller p, and $\mathbf{F}_{\text{prop}}, \mathbf{P}_{\text{prop}} \in \mathbb{R}^{n_{\text{p}} \times n_{\text{t}}}_+$ contain the thrust and power of each propeller. Because propeller rotational speed is not an explicit decision variable, the power surrogate alone does not exclude thrust and advance-speed combinations that require a rotational speed above the rotational-speed limit. During surrogate construction, each sampled pair is classified using the rotational speed required by the B-series model, and a conservative affine maximum-thrust boundary is fitted. The admissible propulsion domain is then enforced by

$$F^{p,t}_{\text{prop}} \leq \gamma^p_0 + \gamma^p_1 u^t_{\text{a}}, \quad \forall p \in \{0, 1, \ldots, n_{\text{p}} - 1\},\ \forall t \in \mathcal{T}^\delta \setminus \mathcal{T}^\delta_{\text{port}}, \tag{55}$$

where $\gamma^p_0, \gamma^p_1 \in \mathbb{R}$ are the fitted boundary coefficients. For the case studies of Section 3.1, the fitting domains contain only feasible sampled points, so the boundary excludes no sampled feasible points. During sailing intervals, total propeller thrust must overcome total resistance:

$$\sum_{p=0}^{n_{\text{p}}-1} F^{p,t}_{\text{prop}} \geq r^t_{\text{tot}} \quad \forall t \in \mathcal{T}^\delta \setminus \mathcal{T}^\delta_{\text{port}}. \tag{56}$$

At ports, propeller thrust and power are set to zero:

$$F_{\text{prop}}^{p,t} = 0, \quad P_{\text{prop}}^{p,t} = 0, \quad \forall p \in \{0, 1, \ldots, n_{\text{p}} - 1\},\ \forall t \in \mathcal{T}_{\text{port}}^{\delta}. \tag{57}$$

Propellers are bounded by their operating power limits $\overline{\mathbf{p}}_{\text{prop}} \in \mathbb{R}_{+}^{n_{\text{p}}}$:

$$P_{\text{prop}}^{p,t} \le \overline{p}_{\text{prop}}^{p}, \quad \forall p \in \{0, 1, \ldots, n_{\text{p}} - 1\}, \quad \forall t \in \mathcal{T}^{\delta}. \tag{58}$$

2.4 Hybrid power system and objective

Onboard photovoltaic power depends only on experienced solar irradiance. To permit curtailment, photovoltaic power $\mathbf{p}_{\text{pv}} \in \mathbb{R}_{+}^{n_{\text{t}}}$ is bounded for area $a_{\text{pv}} \in \mathbb{R}_{+}$ and conversion efficiency $\eta_{\text{pv}} \in [0, 1]$ by

$$p_{\text{pv}}^{t} \le \eta_{\text{pv}} a_{\text{pv}} i^{t}, \quad \forall t \in \mathcal{T}^{\delta}. \tag{59}$$

We use the convex battery model described in [35]. Consider $n_{\text{b}} \in \mathbb{N}$ onboard batteries, modelled with stored energy $\mathbf{E} \in \mathbb{R}_{+}^{n_{\text{b}} \times (n_{\text{t}}+1)}$, a discharge power $\mathbf{P}_{\text{dis}} \in \mathbb{R}_{+}^{n_{\text{b}} \times n_{\text{t}}}$, a charging power $\mathbf{P}_{\text{ch}} \in \mathbb{R}_{+}^{n_{\text{b}} \times n_{\text{t}}}$, charging and discharging efficiencies $\boldsymbol{\eta}_{\text{dis}}, \boldsymbol{\eta}_{\text{ch}} \in [0, 1]^{n_{\text{b}}}$, and a leak coefficient $\boldsymbol{\alpha} \in [0, 1]^{n_{\text{b}}}$. Consider also nonnegative operating limits $\underline{\mathbf{E}}, \overline{\mathbf{E}} \in \mathbb{R}_{+}^{n_{\text{b}} \times (n_{\text{t}}+1)}$ and $\underline{\mathbf{P}}_{\text{dis}}, \overline{\mathbf{P}}_{\text{dis}}, \underline{\mathbf{P}}_{\text{ch}}, \overline{\mathbf{P}}_{\text{ch}} \in \mathbb{R}_{+}^{n_{\text{b}} \times n_{\text{t}}}$. The battery dynamics and power limits are:

$$E^{b,t+1} = (\alpha^{b})^{\delta} E^{b,t} - \delta \frac{P_{\text{dis}}^{b,t}}{\eta_{\text{dis}}^{b}} + \delta \eta_{\text{ch}}^{b} P_{\text{ch}}^{b,t}, \tag{60a}$$

$$\underline{P}_{\text{dis}}^{b,t} \le P_{\text{dis}}^{b,t} \le \overline{P}_{\text{dis}}^{b,t}, \qquad \underline{P}_{\text{ch}}^{b,t} \le P_{\text{ch}}^{b,t} \le \overline{P}_{\text{ch}}^{b,t}, \tag{60b}$$

Let e_{i} and e_{f} denote the parameterized initial and final stored energy. We impose:

$$\underline{E}^{b,t} \le E^{b,t} \le \overline{E}^{b,t}, \forall t \in \mathcal{T},\ \forall b \in \{0, 1, \ldots, n_{\text{b}} - 1\}, \tag{61}$$

$$E^{b,0} = e_{\text{i}}, \quad E^{b,n_{\text{t}}} = e_{\text{f}}, \quad \forall b \in \{0, 1, \ldots, n_{\text{b}} - 1\}. \tag{62}$$

The case studies use fixed commercial schedules, so shore power availability $B^{c,t} \in \{0, 1\}$ is precomputed from scheduled port calls. Let $\mathbf{P}_{\text{sh}} \in \mathbb{R}_{+}^{n_{\text{sh}} \times n_{\text{t}}}$ denote the power purchased from each station and $\overline{\mathbf{P}}_{\text{sh}} \in \mathbb{R}_{+}^{n_{\text{sh}} \times n_{\text{t}}}$ its availability limits, leading to the following constraint:

$$0 \le P_{\text{sh}}^{c,t} \le B^{c,t} \overline{P}_{\text{sh}}^{c,t}, \quad \forall c \in \{0, 1, \ldots, n_{\text{sh}} - 1\}, \quad \forall t \in \mathcal{T}^{\delta}. \tag{63}$$

We represent the shipboard electrical network through an aggregate active-power balance and assume ohmic distribution losses to be negligible, consistent with prior shipboard power-management models that justify this approximation by the short cable and bus-bar runs between onboard generators and loads [36]. Let $n_{\text{g}} \in \mathbb{N}$ denote the number of onboard generators, $\mathbf{P}_{\text{gen}} \in \mathbb{R}_{+}^{n_{\text{g}} \times n_{\text{t}}}$ their active power outputs, and $\mathbf{p}_{\text{a}} \in \mathbb{R}_{+}^{n_{\text{t}}}$ the forecast auxiliary load. The power balance is:

$$\sum_{g=0}^{n_{\text{g}}-1} P_{\text{gen}}^{g,t} + \sum_{c=0}^{n_{\text{sh}}-1} P_{\text{sh}}^{c,t} + \sum_{b=0}^{n_{\text{b}}-1} P_{\text{dis}}^{b,t} + p_{\text{pv}}^{t} = \sum_{p=0}^{n_{\text{p}}-1} P_{\text{prop}}^{p,t} + p_{\text{a}}^{t} + \sum_{b=0}^{n_{\text{b}}-1} P_{\text{ch}}^{b,t}, \quad \forall t \in \mathcal{T}^{\delta}. \tag{64}$$

We include generation operating limits $\underline{P}_{\text{gen}}^{g}, \overline{P}_{\text{gen}}^{g} \in \mathbb{R}_{+}$:

$$\underline{P}_{\text{gen}}^{g} \le P_{\text{gen}}^{g,t} \le \overline{P}_{\text{gen}}^{g} \quad \forall g \in \{0, 1, \ldots, n_{\text{g}} - 1\}, \quad \forall t \in \mathcal{T}^{\delta}. \tag{65}$$

The case studies minimize total energy costs. Generator costs are represented by per-generator quadratic functions with coefficients $\boldsymbol{\kappa}_2, \boldsymbol{\kappa}_1, \boldsymbol{\kappa}_0 \in \mathbb{R}^{n_{\text{g}}}$ and constant fuel price $\pi_{\text{fuel}} \in \mathbb{R}_{+}$. $\boldsymbol{\kappa}_2 \ge 0$ and $\boldsymbol{\kappa}_1 \ge 0$ for convexity and monotonicity. Shore power costs depend on electricity prices $\boldsymbol{\Pi} \in \mathbb{R}_{+}^{n_{\text{sh}} \times n_{\text{t}}}$, which can vary over time and across stations. Let $\mathcal{Y}$ denote the decision variable set of the selected mode. The objective is:

$$f(\mathcal{Y}) = \sum_{t=0}^{n_{\text{t}}-1} \sum_{g=0}^{n_{\text{g}}-1} \left(\kappa_2^{g} (P_{\text{gen}}^{g,t})^2 + \kappa_1^{g} P_{\text{gen}}^{g,t} + \kappa_0^{g} \right) \delta \pi_{\text{fuel}} + \sum_{t=0}^{n_{\text{t}}-1} \sum_{c=0}^{n_{\text{sh}}-1} \left(\Pi^{c,t} P_{\text{sh}}^{c,t} \right) \delta. \tag{66}$$

2.5 Complete MICP models

The four models are presented below for completeness.

2.5.1 JoPSPo-C

The `JoPSPo-C` model is

$$
\begin{aligned}
\min_{\mathcal{Y}_{\text{JoPSPo-C}}} \quad & f(\mathcal{Y}) & & \\
\text{s.t.} \quad & (1), (2), (3), (4), (5), (6), (7), (8), (9), (10), & & \} \text{ navigation and environment} \\
& (11), (12), (14), (15), (16), (17), (18), (19) & & \} \text{ path model} \\
& (47), (49), (50), (53), (54), (55), (56), (57), (58), & & \} \text{ resistance and propulsion} \\
& (59), (60), (61), (62), (63), (64), (65). & & \} \text{ hybrid power system}
\end{aligned}
$$

2.5.2 JoPSPo-D

The constraints below are interpreted for `JoPSPo-D` according to the indexing convention of Section 2.2.5. The model is given by:

$$
\begin{aligned}
\min_{\mathcal{Y}_{\text{JoPSPo-D}}} \quad & f(\mathcal{Y}) & & \\
\text{s.t.} \quad & (1), (2), (3), (5), (6), (7), (8), (9), (10), & & \} \text{ navigation and environment} \\
& (20), (22), (23), (25), (26), (28), & & \} \text{ path model} \\
& (47), (49), (50), (53), (54), (55), (56), (57), (58), & & \} \text{ resistance and propulsion} \\
& (59), (60), (61), (62), (63), (64), (65). & & \} \text{ hybrid power system}
\end{aligned}
$$

2.5.3 FiPSPo-ST

The `FiPSPo-ST` model is written as

$$
\begin{aligned}
\min_{\mathcal{Y}_{\text{FiPSPo-ST}}} \quad & f(\mathcal{Y}) & & \\
\text{s.t.} \quad & (3), (5), (6), (7), (8), (9), (10), (19), & & \} \text{ navigation and environment} \\
& (29), (30), (31), (32), (33), (34), (35), (36), (37), (38), (39), & & \} \text{ path model} \\
& (47), (49), (51), (53), (54), (55), (56), (57), (58), & & \} \text{ resistance and propulsion} \\
& (59), (60), (61), (62), (63), (64), (65). & & \} \text{ hybrid power system}
\end{aligned}
$$

2.5.4 FiPSPo-TI

The `FiPSPo-TI` model is provided by

$$
\begin{aligned}
\min_{\mathcal{Y}_{\text{FiPSPo-TI}}} \quad & f(\mathcal{Y}) & & \\
\text{s.t.} \quad & (7), (9), & & \} \text{ navigation and environment} \\
& (29), (30), (32), (42), (43), (44), (46), & & \} \text{ path model} \\
& (47), (49), (52), (53), (54), (55), (56), (57), (58), & & \} \text{ resistance and propulsion} \\
& (59), (60), (61), (62), (63), (64), (65). & & \} \text{ hybrid power system}
\end{aligned}
$$

When spatially varying speed limits are imposed, `FiPSPo-TI` additionally includes (3), (8), (10), and (31).

3 Numerical case studies

All experiments are run on a laptop computer equipped with a 13th-generation Intel Core i9-13900HX processor and 32 GB of RAM. Models are implemented in `CVXPY` 1.7.3 and solved with `MOSEK` 11.0.22 using a 12 h time limit and its default relative optimality tolerance [37]. Code and data-processing scripts are available in the `CVXship` repository [38].

3.1 Test cases

We illustrate the performance of our models through four specific test cases:

Case # 1: Halifax, NS to Grande-Entrée, QC, with an added synthetic storm adapts the synthetic experiment of [31] to test whether decision-dependent space-time models can exploit schedule flexibility to avoid a short-lived local disturbance. The case is a controlled stress test rather than an estimate of real-world savings. Relative to Case # 2, adverse winds of 30 m/s and currents of 2 m/s are imposed in set 2 from 18:00 to 21:00, coinciding with the reference trajectory's passage. All other data, parameters, and set partitions match Case # 2.

Case # 2: Halifax, NS to Grande-Entrée, QC, evaluates the methods when path flexibility has limited value because the best path is expected to remain near the shortest navigable path. As shown in Figure 1a, the region is represented by five ordered convex sets that preserve direct paths, and no speed limits are imposed.

Case # 3: Sept-Îles, QC, to Grosse Île, QC, evaluates routing under the 10 kn seasonal restrictions designated in the Gulf of St. Lawrence [39]. As shown in Figure 1b, the partition follows the regulatory boundaries and merges adjacent regions subject to the same limit. The schedule creates a trade-off between accelerating outside the restricted area and detouring around it.

Case # 4: Freeport, Bahamas to Southport, North Carolina, evaluates whether joint path optimization can trade additional distance for favourable Gulf Stream currents. The set partition separates the Gulf Stream core from surrounding waters with weaker currents, as shown in Figure 1c.

3.2 Parameters

Parameters and variables use different units to keep their numerical magnitudes near unity and improve numerical conditioning. The implementation applies the required unit conversions, although the corresponding conversion factors are omitted from Section 2 for readability. Historical ocean currents and atmospheric fields are obtained from Copernicus Marine [40] and ERA5 [41], respectively. They are treated as perfectly known deterministic forecasts. Forecast uncertainty is outside the scope of the study. For each case, 1 km GMRT bathymetry [42] is compared with the minimum navigable depth to define navigable waters. Convex sets are constructed manually to preserve direct paths, separate strong environmental gradients, and isolate speed-restricted regions. All voyages depart at 06:00 UTC to standardize schedules and include daytime solar availability. Table 1 reports the sailing times and departure dates. All voyages include a 3 h port call at both the origin and the destination. The auxiliary load is 0.3 MW, the fuel price is 1.2155 USD/kg, and the initial and terminal battery states of charge are 50% and 100%, respectively. Shore power is assumed available at all ports up to 2 MW. Scenario shore-power prices reported in Table 2 are representative marginal energy prices approximated from local utility tariffs. [43–47]. Canadian prices are converted at 1 CAD = 0.71 USD, while the Bahamian dollar is assumed at parity with the US dollar [48, 49]. The reported coordinates are not exact port positions. `FiPSPo-TI` uses five iterations, initialized from the `SPaCS` trajectory.

3.2.1 Ship

All cases use the S-175 containership hull under a fixed loading condition [50]. The Blendermann wind coefficients are taken from [33], and the projected windage areas are taken from [51]. Table 3

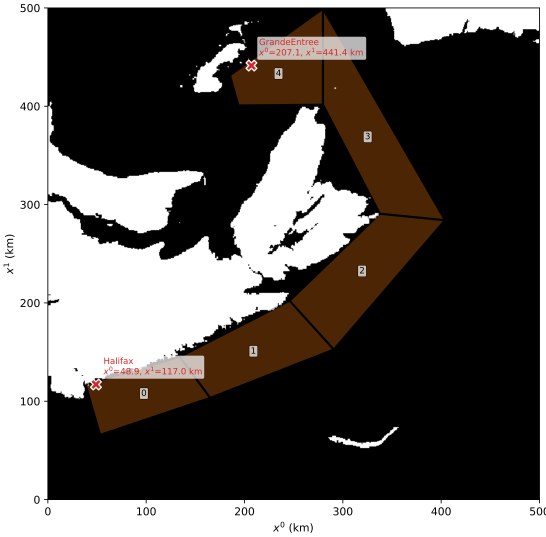

(a) Halifax to Grande-Entrée.

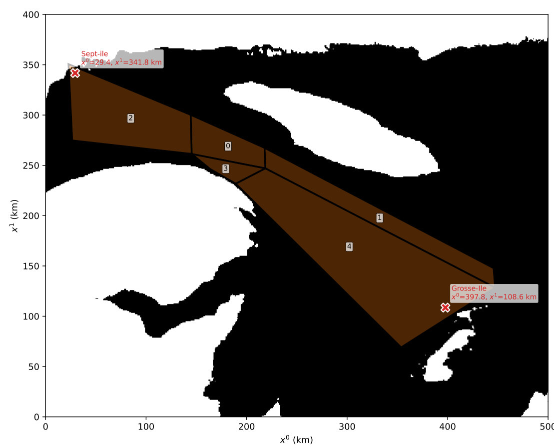

(b) Sept-Îles to Grosse Île.

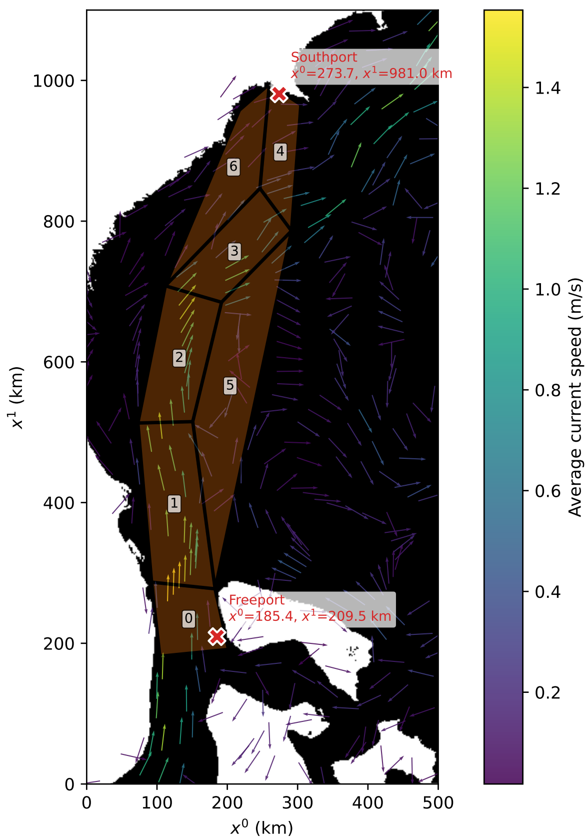

(c) Freeport to Southport.

Figure 1: Test-case convex set partitions.

Table 1: Schedules.

Case	#1	#2	#3	#4
Sail time (h)	30	30	20	38
Departure date 1	2025-01-01	2025-01-01	2025-05-01	2025-01-01
Departure date 2	N/A	2025-03-01	2025-05-31	2025-03-01
Departure date 3	N/A	2025-07-01	2025-06-28	2025-07-01
Departure date 4	N/A	2025-09-01	N/A	2025-09-01
Departure date 5	N/A	2025-11-01	N/A	2025-11-01

reports the main hull parameters. The twin-screw fixed-pitch propulsion system is adapted from the optimized Wageningen B-series configuration of [52]. The power system comprises two Caterpillar M 25 E variable-speed generator sets, a 3 MWh battery with 0.7C charge and discharge limits, and 1500 m^2 of photovoltaic panels. Generator fuel curves are fitted to manufacturer data [53]. Tables 4 and 5 report the complete parameterization.

Table 2: Port parameters.

Port	**(latitude, longitude)**	**Shore power price (USD/MWh)**
Grande-Entrée	(47.4398, −61.2564)	79.11
Halifax	(44.5514, −63.3844)	79.04
Sept-Îles	(50.0687, −66.2570)	79.11
Freeport	(26.6989, −79.1371)	363.50
Southport	(33.6406, −78.0610)	215.00
Grosse Île	(47.9655, −61.7804)	79.11

Table 3: Ship parameters.

Parameter	**Value**	**Unit**
Minimum navigable depth	15.525	m
Beam	25.4	m
Waterline length	175	m
Draught	9.5	m
Block coefficient	0.572	–
Lateral projected windage area	3710	m^2
Frontal projected windage area	756	m^2
Wetted hull area	4927.6	m^2
Wind coefficients	0.9, 0.55, 0.55, 0.4	–
Maximum ship speed ($\overline{v}$)	11.27	m/s

Table 4: Propulsion-system parameters.

Parameter	**Value**	**Unit**
Diameter	5.00	m
Pitch	3.96	m
Pitch-to-diameter ratio	0.792	–
Expanded blade-area ratio	0.62	–
Number of blades	6	–
Wake fraction	0.3	–
Maximum rotational speed	2.05	rps
Maximum shaft power per propeller	2.67	MW
Number of propellers	2	–

Table 5: Power system parameters.

Parameter	**Symbol**	**Value**	**Unit**
Battery capacity	$\overline{E}$	3	MWh
Battery charge limits	$\underline{P}_{\text{ch}}, \overline{P}_{\text{ch}}$	0, 2.1	MW
Battery discharge limits	$\underline{P}_{\text{dis}}, \overline{P}_{\text{dis}}$	0, 2.1	MW
Battery charge efficiency	η_{ch}	0.95	–
Battery discharge efficiency	η_{dis}	0.95	–
Leakage factor per hour	α	0.999958	–
Solar panel area	a_{pv}	1500	m^2
Solar panel efficiency	η_{pv}	0.24	–
Per generator maximum power	$\overline{P}^{g}_{\text{gen}}$	2.8	MW
Fuel curve parameter	κ_0	17.64197	kg/h
Fuel curve parameter	κ_1	159.86845	kg/MWh
Fuel curve parameter	κ_2	7.74853	kg/(MW^2h)
Number of generators	n_{g}	2	–

3.3 Benchmarks

The comparison is restricted to MICP methods because the objective is to isolate the value of joint path, speed, and power optimization within models for which global optimality can be certified. All methods use the same convex set decomposition and common physical, operational, and economic models.

- `SPaCS` is a rule-based baseline that requires neither optimization nor environmental forecasts. It follows the shortest feasible path and selects a common cruising speed, capped by local speed limits, that satisfies the schedule. At ports, `SPaCS` prioritizes solar generation and charges the battery using shore power subject to the applicable power and state-of-charge limits. During sailing, it applies a uniform battery-discharge command. The common evaluator described in Section 3.4 subsequently supplies any generation required to restore power balance.
- `Greedy` uses the `SPaCS` path and speed profile but dispatches sailing power in the order solar generation, battery discharge, and generator. This policy prioritizes the currently cheapest available source without anticipating future operating conditions. Its port policy is identical to that of `SPaCS`.
- Fixed Path joint speed-power optimization with spatially averaged environment (`FiPSPo-SA`) is identical to `FiPSPo-TI`, except that environmental conditions vary with time but are spatially uniform at each time step. At each time step, it averages values interpolated at ten equally spaced points along the fixed path. This provides a common-model proxy for the spatially uniform treatment of environmental conditions in previous joint speed-power studies [13–16].

3.4 Common feasibility-restoration evaluation method

The optimization models use spatially aggregated environmental inputs and convex surrogates, so their solutions may be infeasible for the original nonconvex problem. For a fair comparison, the evaluation interpolates environmental conditions at the spatial and temporal midpoint of each trajectory segment, and nonlinear resistance and propulsion power are recomputed with the original nonlinear models without changing the planned path or speed. A common controller then restores power balance by adjusting shore power, generator output, battery charging and discharging, and solar curtailment in a fixed priority order. This feasibility-restoration controller would be deployed in practice to maintain the power balance. It subsequently restores the terminal battery state of charge by buying enough shore power, which would be done in practice as well. Solutions that cannot be restored are classified as infeasible. The complete procedure is provided in B.

4 Numerical results

All solutions are evaluated after applying the feasibility restoration procedure described in Section 3.4. For each departure date and time step, the evaluated savings of method m relative to `SPaCS` are $100(J^{\texttt{SPaCS}} - J^m)/J^{\texttt{SPaCS}}$, where J denotes evaluated operating cost. Positive values favour method m. Case # 1 contains one departure date, the other entries are means. Highest displayed mean in each column is bold. Tables 6, 7, and 8 report the evaluated savings at the three tested time-step resolutions. Reported computation times correspond to producing a complete optimized voyage plan over the full scheduled horizon. They include compilation and optimization, including all five `FiPSPo-TI` iterations, but exclude offline data processing and solution evaluation. The notation `TL` indicates that no evaluated solution is reported within the 12 h computation limit.

Table 6: Evaluated operating cost savings relative to SPaCS at $\delta = 1$ h [%].

Method	Case 1	Case 2	Case 3	Case 4
Greedy	−0.30	−0.24	*Infeasible*	−0.06
FiPSPo-SA	4.09	**0.59**	1.31	3.75
FiPSPo-TI	9.61	0.57	1.30	3.77
FiPSPo-ST	13.38	0.15	1.30	3.14
JoPSPo-C	12.51	0.14	**14.22**	**5.92**
JoPSPo-D	**15.30**	0.31	13.66	3.68

Table 7: Evaluated operating cost savings relative to SPaCS at $\delta = 30$ min [%].

Method	Case 1	Case 2	Case 3	Case 4
Greedy	−0.42	−0.37	*Infeasible*	−0.05
FiPSPo-SA	4.39	**1.08**	1.63	**3.68**
FiPSPo-TI	9.85	1.07	1.63	**3.68**
FiPSPo-ST	15.78	0.84	**1.64**	3.53
JoPSPo-C	14.90	0.76	TL	TL
JoPSPo-D	**16.60**	0.71	TL	TL

Table 8: Evaluated operating cost savings relative to SPaCS at $\delta = 15$ min [%].

Method	Case 1	Case 2
Greedy	−0.44	−0.40
FiPSPo-SA	4.46	1.16
FiPSPo-TI	9.94	**1.17**
FiPSPo-ST	16.36	0.88
JoPSPo-C	16.08	0.89
JoPSPo-D	**16.89**	0.88

4.1 Value of space-time environmental coupling

Case # 1 isolates the value of coupling passage time with local environmental conditions. At $\delta =$ 15 min, FiPSPo-SA and FiPSPo-TI save 4.46% and 9.94%, respectively, whereas the decision-dependent space-time models save between 16.08% and 16.89%. As illustrated in Figure 2, FiPSPo-TI adjusts speed while traversing the disturbed region (coloured area), but does not move its passage outside the 18:00-21:00 disturbance window. In contrast, FiPSPo-ST, JoPSPo-C, and JoPSPo-D reduce speed before entering the affected set 2 and delay passage until the disturbance has subsided. Because the fixed-path FiPSPo-ST model nearly matches the joint models in this case, most of the improvement arises from decision-dependent passage timing rather than path flexibility. The synthetic disturbance deliberately amplifies this effect and should not be interpreted as an estimate of typical real-world savings.

The benefit of trajectory-indexed interpolation is smaller in the historical data cases. Across Cases 2-4, the mean savings obtained by FiPSPo-SA and FiPSPo-TI differ by at most 0.02% at every tested resolution. Thus, trajectory-indexed environmental inputs provide no material improvement over spatial averaging in the historical conditions considered here. In Case # 2, where the shortest navigable path is already favourable, all optimization-based methods save only 0.88-1.17% at $\delta =$ 15 min, and the models that do not rely on set-averaged environmental conditions perform slightly better.

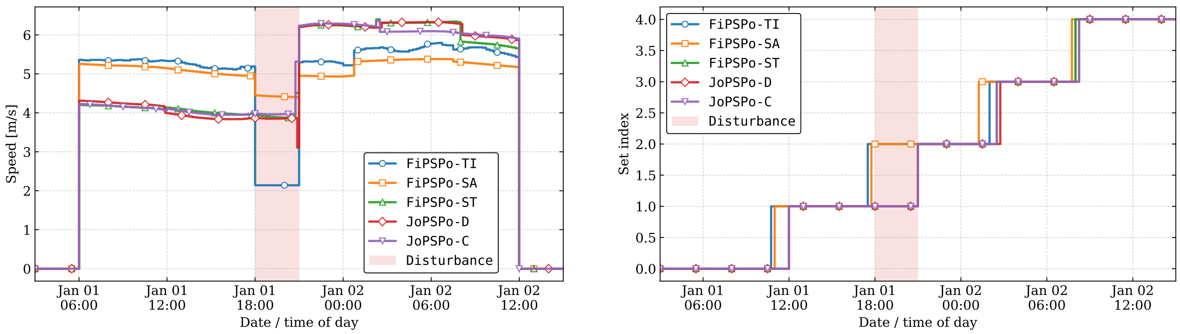

(a) Speed magnitude.

(b) Convex set occupancy.

Figure 2: Responses to the synthetic disturbance for the 2025-01-01 departure in Case # 1.

4.2 Value of joint path optimization

Path flexibility is decisive in Case # 3. At $\delta = 1$ h, the three fixed-path models save approximately 1.3%, whereas `JoPSPo-C` and `JoPSPo-D` save 14.22% and 13.66%, respectively. Across the three departure dates, their savings remain between 11.26% and 16.76% for `JoPSPo-C` and between 10.22% and 17.06% for `JoPSPo-D`. As shown in Figures 3a and 3b, the joint models can trade additional distance for reduced exposure to the speed restricted region, whereas fixed-path methods must compensate by travelling faster outside it. In Case # 4, `JoPSPo-C` obtains the largest mean saving, 5.92%, compared with 3.77% for the best fixed-path result. Its savings vary from 2.75% to 9.81% across departure dates, reflecting the time varying value of routing through favourable Gulf Stream currents. However, `JoPSPo-D` averages 3.68% and ranges from -0.96% to 7.12%. Path flexibility can therefore provide substantial value, but evaluated performance also depends on how convex set transitions are represented. In some Case # 4 transitions, `JoPSPo-C` places $\mathbf{x}^{t+1}$ just inside a favourable-current set and $\mathbf{q}^t$ almost at the same boundary location. The second leg then covers negligible distance, but the equal-leg current approximation in (17) still assigns it a half-interval contribution from the favourable current, artificially improving the modelled objective. The nonlinear evaluation reconstructs the actual leg durations and corrects this mismatch. This approximation competes with `JoPSPo-D`'s restriction of transitions to half-time step instants, so neither model consistently dominates. At $\delta = 1$ h, `JoPSPo-D` produces higher mean savings in Cases 1 and 2, whereas `JoPSPo-C` produces higher mean savings in Cases 3 and 4.

4.3 Temporal resolution and computational trade-offs

The evaluated results of the three decision-dependent space-time models improve, and become closer as the time step is shortened. In Case # 1, the spread between the mean savings of `FiPSPo-ST`, `JoPSPo-C`, and `JoPSPo-D` decreases from 2.79 percentage points at $\delta = 1$ h to 1.70 at $\delta = 30$ min and 0.81 at $\delta = 15$ min. In Case # 2, the corresponding spread decreases from 0.17 to 0.13 and then 0.01 percentage points. This pattern is consistent with shorter time steps reducing the influence of transition averaging in `FiPSPo-ST` and `JoPSPo-C` while refining the admissible transition time grid of `JoPSPo-D`. Table 9 reports mean computation times at the common $\delta = 1$ h resolution. `FiPSPo-SA` and `FiPSPo-TI` solve in less than 5 s in every case. In comparison, `FiPSPo-ST` requires between 3.72 and 116 s, while the joint models require between 100 and 1 140 s. The computational burden grows sharply under time step refinement. At $\delta = 15$ min, the mean computation times of `FiPSPo-ST`, `JoPSPo-C`, and `JoPSPo-D` range from 2 920 to 6 555 s in Case # 1 and from 5 328 to 12 932 s in Case # 2. By contrast, `FiPSPo-SA` and `FiPSPo-TI` remain below 27 s. At $\delta = 30$ min, neither joint model produces a reported evaluated solution within the 12 h limit in Cases 3 and 4. Finer temporal resolution therefore improves solutions and reduces differences among the advanced models, but at a steep computational cost.

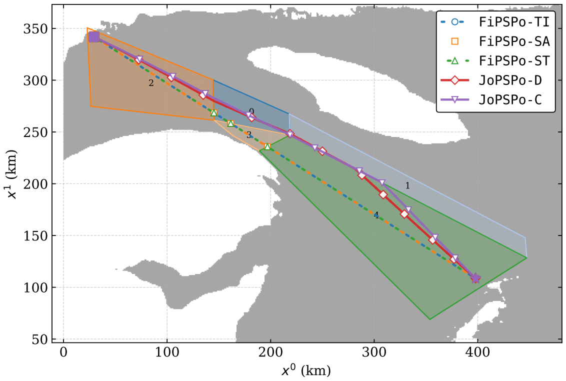

(a) Case # 3 paths, departure 2025-05-01.

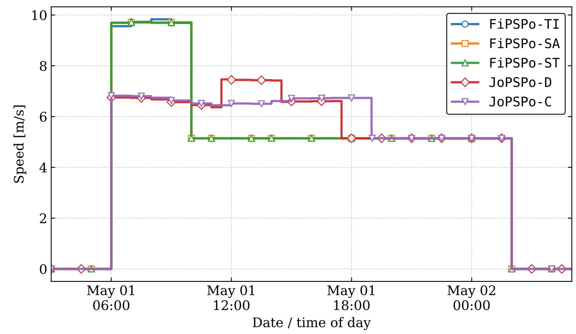

(b) Case # 3 speed profiles, departure 2025-05-01.

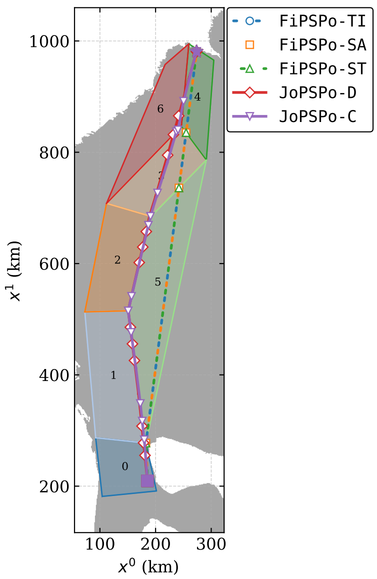

(c) Case # 4 paths, departure 2025-01-01.

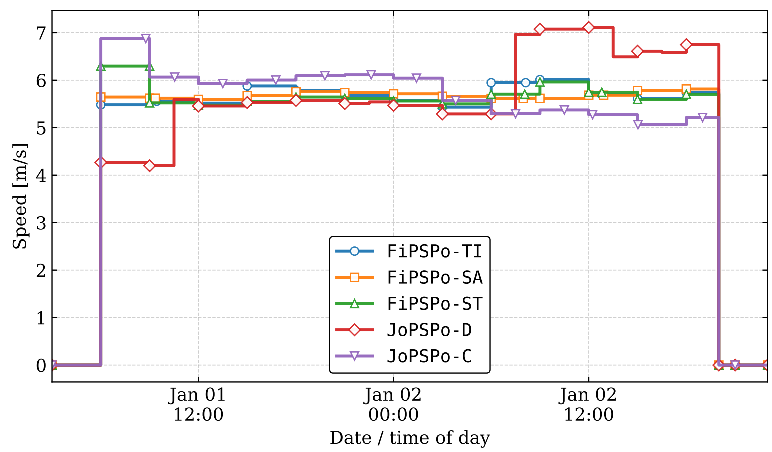

(d) Case # 4 speed profiles, departure 2025-01-01.

Figure 3: Representative paths and planned speed profiles in the two path-sensitive cases at $\delta = 1$ h.

Table 9: Mean computation times at $\delta = 1$ h (s).

Method	Case 1	Case 2	Case 3	Case 4
`Greedy`	0.66	0.63	0.55	0.33
`FiPSPo-SA`	0.96	0.82	0.76	0.38
`FiPSPo-TI`	4.33	3.97	3.87	1.82
`FiPSPo-ST`	116	105	3.72	10.6
`JoPSPo-C`	113	100	581	998
`JoPSPo-D`	184	111	1 140	147

5 Conclusion

This work introduces the first mixed-integer convex program (MICP) model for jointly optimizing a continuous two-dimensional ship path, speed profile, and hybrid power system operation under spatially and temporally varying conditions. The navigable domain is decomposed into interconnected obstacle-free convex sets, and time-indexed binary variables both enforce navigability and activate the currents, winds, solar irradiance, and speed limits associated with the ship's position and passage time. Two free-path formulations are developed: joint path-speed-power optimization with continuous speed (`JoPSPo-C`) and joint path-speed-power optimization with discrete speed (`JoPSPo-D`). Two fixed-path formulations are also developed: fixed-path joint speed-power optimization with space-time environment (`FiPSPo-ST`), and fixed-path joint speed-power optimization with trajectory-indexed environment (`FiPSPo-TI`). These four models provide different trade-offs between modelling fidelity and computational complexity. They are coupled with convex resistance and propulsion surrogates, including a free-heading approximation of Blendermann wind resistance, and with models of batteries, photovoltaic generation, shore power, and diesel generators. The resulting models can be solved to certified global optimality using off-the-shelf solvers. The numerical results show that the value of this additional modelling flexibility is case-dependent. In the synthetic stress test, the decision-dependent space-time models delay passage through a short-lived adverse region and reduce evaluated operating cost by up to 16.89% relative to a shortest-path constant-speed (`SPaCS`) benchmark. When the shortest path is already favourable, all optimization-based methods provide savings of approximately 1%, and the inexpensive fixed-path models offer a better trade-off between solution quality and computation time. By contrast, joint path optimization provides substantial value when path choice changes exposure to spatial constraints. `JoPSPo-C` achieves average savings of 14.22% under spatially varying vessel-speed restrictions and 5.92% near the Gulf Stream, compared with approximately 1.3% and 3.77%, respectively, for the best fixed-path results. Shorter time steps improve solutions and reduce differences among the advanced models, but the associated increase in binary variables produces a steep computational cost and prevents the joint models from returning evaluated solutions within 12 hours in the more complex cases at $\delta = 30$ min, making this mitigation unsuitable for online utilization. Therefore, no model dominates across the tested cases. `JoPSPo-C` and `JoPSPo-D` are best when speed restrictions or strong spatial current gradients make path selection central to the problem while fixed-path models are preferable when the shortest path is already favourable. `FiPSPo-ST` is most relevant when decision-dependent passage timing matters, but path flexibility is unnecessary. Future work should account for forecast uncertainty using robust or stochastic extensions.

6 CRediT authorship contribution statement

Louis-Philippe Baillargeon: Writing – review & editing, Writing – original draft, Visualization, Validation, Software, Methodology, Conceptualization. **Maxime Berger:** Writing – review & editing, Supervision, Methodology, Validation, Resources, Funding acquisition, Conceptualization. **Antoine Lesage-Landry:** Writing – review & editing, Supervision, Methodology, Validation, Resources, Funding acquisition, Conceptualization.

7 Declaration of competing interest

The authors declare that they have no known competing financial interests or personal relationships that could have appeared to influence the work reported in this paper.

Appendix A Convex surrogates

The problem-specific surrogate fitting domains are obtained by scaling the minimum and maximum ship speed, total resistance, and propulsion power values in the `SPaCS` solution using the factors in Table A.1. The calm-water surrogate is instead fitted over the full admissible speed range.

Figure A.1 compares the Molland model, the nominal-speed quadratic approximation, and the fitted convex polynomial for the S-175 parameters of Section 3.2.1. The polynomial yields lower mean and maximum sampled absolute errors than the quadratic approximation as reported in Table A.2. Figures A.2, A.3, and A.4 show the fits with the largest sampled absolute error for the one-dimensional, path-aligned two-dimensional, and unrestricted two-dimensional surrogates, respectively. Table A.3 reports the corresponding aggregate errors.

Table A.1: Scale factors applied to the SPaCS extrema to define the problem-specific surrogate fitting domains.

Scale factor	Case 1	Case 2	Case 3	Case 4
Ship speed, lower	0.50	0.90	0.90	0.90
Ship speed, upper	1.15	1.15	1.15	1.25
Total resistance, lower	0.50	0.70	0.70	0.70
Total resistance, upper	1.20	1.20	1.20	1.20
Propulsion power, lower	0.50	0.70	0.70	0.70
Propulsion power, upper	1.20	1.20	1.20	1.20

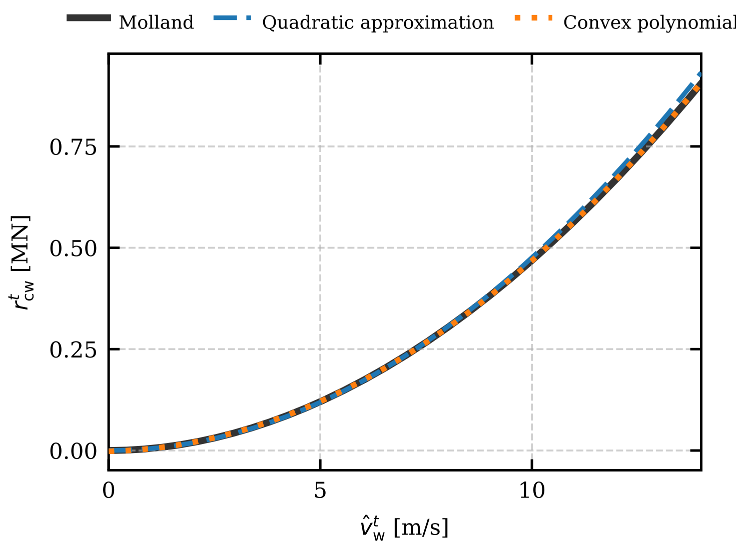

Figure A.1: Comparison of the Molland calm-water resistance model, the nominal-speed quadratic approximation, and the fitted convex polynomial surrogate.

Table A.2: Approximation errors for the convex water resistance models [MN].

Model	Mean absolute error	Maximum absolute error
Convex polynomial	0.000527	0.001948
Nominal-speed quadratic	0.005581	0.026325

Table A.3: Approximation errors for the convex wind resistance models [MN].

Model	Average abs. error	Worst abs. error	Mean abs. resistance
`1D`	5.17×10^{-5}	1.26×10^{-4}	6.61×10^{-2}
`2D-aligned`	2.27×10^{-3}	1.02×10^{-2}	4.44×10^{-2}
`2D`	1.06×10^{-2}	3.49×10^{-2}	6.57×10^{-2}

Figure A.5 compares the nonlinear B-series model and the convex surrogate over the fitted domain for Case # 2, 2025-01-01. The mean absolute error is 4.82×10^{-3} MW, or 1.25% of the mean reference power, and the maximum sampled absolute error is 2.04×10^{-2} MW.

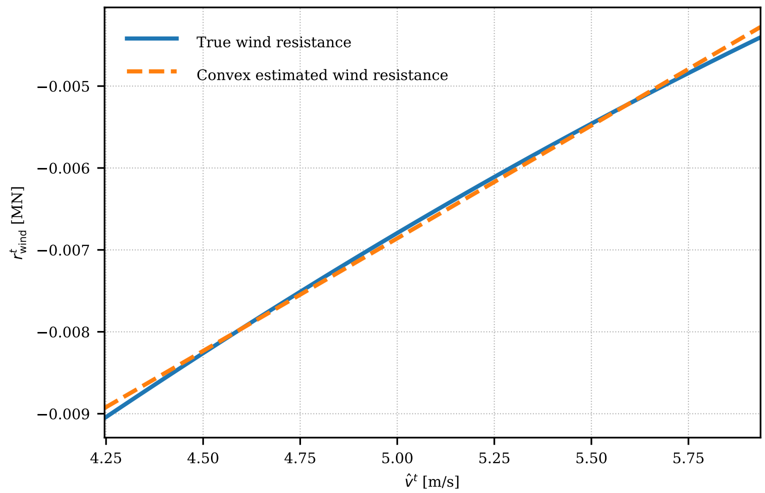

Figure A.2: One-dimensional wind-resistance fit with the largest sampled absolute error, for Case # 2 and departure 2025-01-01.

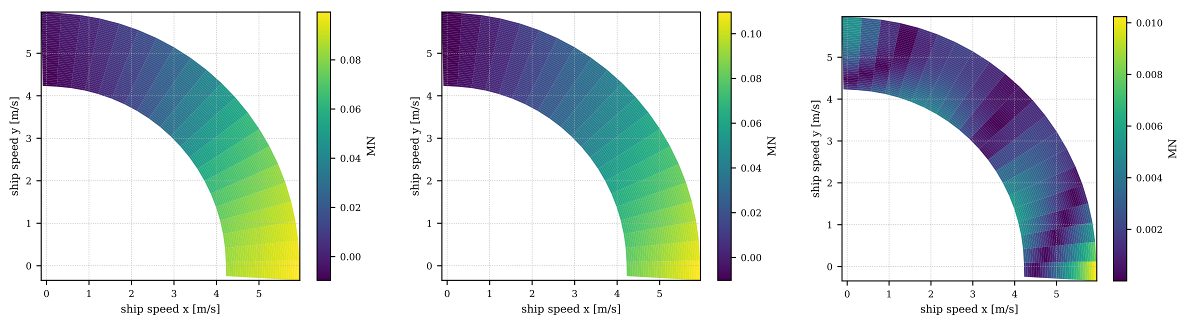

(a) Nonlinear model. **(b) Convex surrogate.** **(c) Absolute error.**

Figure A.3: Path-aligned two-dimensional wind-resistance fit with the largest sampled absolute error for Case # 2 and departure 2025-01-01.

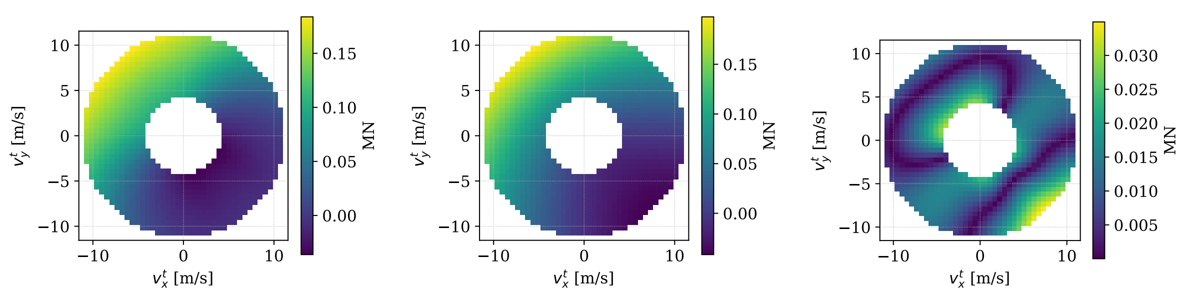

(a) Nonlinear model. **(b) Convex surrogate.** **(c) Absolute error.**

Figure A.4: Unrestricted two-dimensional wind-resistance fit with the largest sampled absolute error for Case # 3 and departure 2025-05-01.

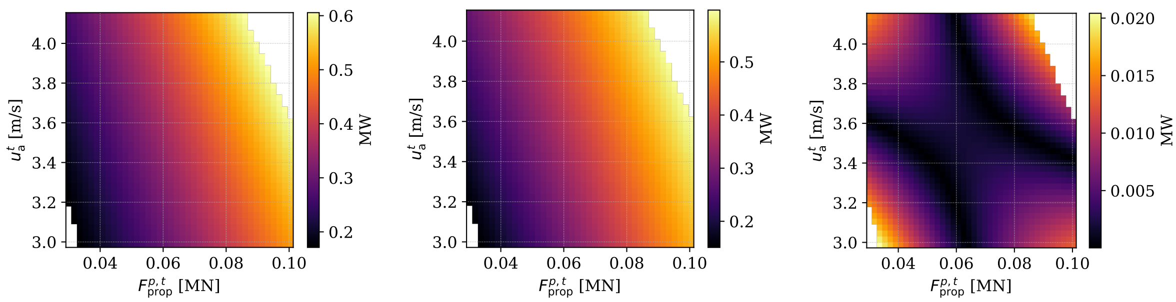

(a) B-series power. **(b) Convex surrogate.** **(c) Absolute error.**

Figure A.5: Propulsion power fit for Case # 2 and departure 2025-01-01.

Appendix B Nonlinear evaluation and feasibility restoration

The planned path and speed profile remain fixed throughout the evaluation. The procedure is as follows:

1. Decompose each interval into constant-heading segments and compute their durations from the planned geometry and speed. Fixed-path methods use the prescribed path, `JoPSPo-C` uses its helper-point legs, and `JoPSPo-D` already provides two fixed half-intervals.
2. At each segment midpoint, interpolate solar irradiance, current, and wind; reconstruct the ground- and water-relative velocities; and recompute resistance and propulsion power using the nonlinear models. Photovoltaic generation is reset to the interpolated availability and curtailed only when necessary.
3. Restore the power balance subject to all device and state-of-charge limits. For a deficit, adjust controls in the order

$$\text{increase } P_{\text{sh}} \rightarrow \text{increase } P_{\text{gen}} \rightarrow \text{decrease } P_{\text{ch}} \rightarrow \text{increase } P_{\text{dis}}.$$

   For a surplus, use

$$\text{decrease } P_{\text{gen}} \rightarrow \text{decrease } P_{\text{sh}} \rightarrow \text{decrease } P_{\text{dis}} \rightarrow \text{increase } P_{\text{ch}} \rightarrow \text{decrease } P_{\text{pv}}.$$

   Generator adjustments are distributed proportionally to their available upward or downward margins.
4. Propagate the battery state of charge. If the terminal target is violated, buy more shore power to increase charge at destination ports. Accept solutions with higher terminal state of charge than necessary.

The evaluated solution is infeasible if a segment's power balance or the terminal state-of-charge target cannot be restored.

References

[1] M. Schmied, W. Knörr, Calculating GHG emissions for freight forwarding and logistics services in accordance with EN 16258: Terms, methods, examples, Tech. rep., European Association for Forwarding, Transport, Logistics and Customs Services (CLECAT) (Apr. 2012). URL https://www.clecat.org/media/CLECAT_Guide_on_Calculating_GHG_emissions_for_freight_forwarding_and_logistics_services.pdf

[2] American Bureau of Shipping, Beyond the horizon: Carbon neutral fuel pathways and transformational technologies, Tech. rep., American Bureau of Shipping (2024). URL https://ww2.eagle.org/en/interactive/interactive-publications/current/outlook-2024.html

[3] J. Kersey, N. D. Popovich, A. A. Phadke, Rapid battery cost declines accelerate the prospects of all-electric interregional container shipping, Nature Energy 7 (7) (2022) 664–674.

[4] T. Solakivi, A. Paimander, L. Ojala, Cost competitiveness of alternative maritime fuels in the new regulatory framework, Transportation Research Part D: Transport and Environment 113 (2022) 103500.

[5] Y. Qiu, C. Yuan, J. Tang, X. Tang, Techno-economic analysis of PV systems integrated into ship power grid: A case study, Energy Conversion and Management 198 (2019) 111925.

[6] Innovation Maritime, L'électrification des quais au Québec, Tech. rep., Innovation Maritime (2022). URL https://tmq.ca/wp-content/uploads/2022/05/Electrification-des-quais-au-Quebec-MeRLIN-IMAR.pdf

[7] H. Helgesen, Study on electrical energy storage for ships: Battery systems for maritime applications—technology, sustainability and safety, Tech. Rep. 2019-0217, Rev. 04, European Maritime Safety Agency, Lisbon, Portugal (May 2020). URL https://www.emsa.europa.eu/publications/item/3895-study-on-electrical-energy-storage-for-ships.html

[8] European Maritime Safety Agency, Guidance on the safety of battery energy storage systems (BESS) on board ships, Tech. Rep. Version 1.0, European Maritime Safety Agency, Lisbon, Portugal (Nov. 2023). URL https://emsa.europa.eu/newsroom/latest-news/download/7643/5065/23.html

[9] A. Fan, K. Ye, K. Li, Z. Yuan, H. Liu, N. Vladimir, W. Mao, Review of speed optimisation for ship energy efficiency: Methods, taxonomy and challenges, Energy 354 (2026) 141138.

[10] Y. Chen, C. Zhang, Y. Guo, Y. Wang, X. Lang, M. Zhang, W. Mao, State-of-the-art optimization algorithms in weather routing: Ship decision support systems: Challenge, taxonomy, and review, Ocean Engineering 331 (2025) 121198.

[11] Y. Yuan, J. Wang, X. Yan, B. Shen, T. Long, A review of multi-energy hybrid power system for ships, Renewable and Sustainable Energy Reviews 132 (2020) 110081.

[12] A. Ritari, N. Katzenburg, F. Oliveira, K. Tammi, Integrated supervisory control and fixed path speed trajectory generation for hybrid electric ships via convex optimization, arXiv:2307.06184 (2023). URL https://arxiv.org/abs/2307.06184

[13] Z. Li, Y. Xu, S. Fang, X. Zheng, X. Feng, Robust coordination of a hybrid AC/DC multi-energy ship microgrid with flexible voyage and thermal loads, IEEE Transactions on Smart Grid 11 (4) (2020) 2782–2793.

[14] F. F. Angkasa, R. Zafar, I.-Y. Chung, Optimal power generation and voyage scheduling in shipboard power systems considering load characteristics-based operating reserve management, Journal of Electrical Engineering & Technology 18 (4) (2023) 2505–2515.

[15] Q. Xu, B. Yang, Y. Yuan, F. Lin, C. Chen, Optimal coordinated generation and demand scheduling for ship hybrid energy system, in: 8th Renewable Power Generation Conference (RPG 2019), 2019, pp. 1–6.

[16] Q. Xu, B. Yang, Q. Han, Y. Yuan, C. Chen, X. Guan, Optimal power management for failure mode of MVDC microgrids in all-electric ships, IEEE Transactions on Power Systems 34 (2) (2019) 1054–1067.

[17] H. Hooshmand, N. Nasiri, S. N. Ravdanegh, Sustainable power management solutions for shipboard power systems: Incorporating CHP, hydrogen fuel cells, battery, and solar energy, Journal of Energy Storage 114 (2025) 115789.

[18] S. Fang, Y. Xu, Multi-objective robust energy management for all-electric shipboard microgrid under uncertain wind and wave, International Journal of Electrical Power & Energy Systems 117 (2020) 105600.

[19] Z. Wang, L. Chen, B. Wang, L. Huang, K. Wang, R. Ma, Integrated optimization of speed schedule and energy management for a hybrid electric cruise ship considering environmental factors, Energy 282 (2023) 128795.

[20] R. Zaccone, E. Ottaviani, M. Figari, M. Altosole, Ship voyage optimization for safe and energy-efficient navigation: A dynamic programming approach, Ocean Engineering 153 (2018) 215–224.

[21] H. Wang, W. Mao, L. Eriksson, A three-dimensional Dijkstra's algorithm for multi-objective ship voyage optimization, Ocean Engineering 186 (2019) 106131.

[22] K. Wang, X. Guo, J. Zhao, R. Ma, L. Huang, F. Tian, S. Dong, P. Zhang, C. Liu, Z. Wang, An integrated collaborative decision-making method for optimizing energy consumption of sail-assisted ships towards low-carbon shipping, Ocean Engineering 266 (2022) 112810.

[23] S. Kuhlemann, K. Tierney, A genetic algorithm for finding realistic sea routes considering the weather, Journal of Heuristics 26 (6) (2020) 801–825.

[24] Y. Zhou, S. Turkmen, K. Pazouki, R. Norman, Route and speed optimisation of a general cargo ship using extreme gradient boosting and enhanced deep Q-network approaches, Transportation Research Part E: Logistics and Transportation Review 206 (2026) 104555.

[25] R. Khatami, B. Chen, Y. C. Chen, Optimal voyage scheduling of all-electric ships considering underwater radiated noise, Transportation Research Part C: Emerging Technologies 148 (2023) 104024.

[26] X. Liu, K. Wang, X. Guo, Z. Li, J. Wu, R. Ma, L. Huang, X. Li, An integrated energy efficiency optimization method of the wind-assisted hybrid ship for the shipping decarbonization, Marine Pollution Bulletin 212 (2025) 117579.

[27] Z. Wang, L. Chen, L. Huang, K. Wang, R. Ma, B. Wang, Adaptive integrated optimization of route, speed, and power flow for a hybrid power cruise ship under time-space varying sea conditions, Energy 356 (2026) 141129.

[28] T. Marcucci, M. Petersen, D. von Wrangel, R. Tedrake, Motion planning around obstacles with convex optimization, Science Robotics 8 (84) (2023) eadf7843. arXiv:https://www.science.org/doi/pdf/10.1126/scirobotics.adf7843.

[29] J. Tang, Z. Mao, L. Yang, H. Ma, Space-time graphs of convex sets for multi-robot motion planning, in: 2025 IEEE/RSJ International Conference on Intelligent Robots and Systems (IROS), IEEE, Hangzhou, China, 2025, pp. 8683–8690.

[30] L. Sun, Y. Zhang, F. Ma, F. Ji, Y. Xiong, Energy and speed optimization of inland battery-powered ship with considering the dynamic electricity price and complex navigational environment, Energy Reports 9 (2023) 293–304, proceedings of the 2022 3rd International Conference on Power Engineering.

[31] S. van Dooren, P. Duhr, C. H. Onder, Convex modelling for ship speed optimisation, Ocean Engineering 288 (2023) 115947.

[32] A. F. Molland, S. R. Turnock, D. A. Hudson, Ship Resistance and Propulsion: Practical Estimation of Ship Propulsive Power, 2nd Edition, Cambridge University Press, Cambridge, UK, 2017.

[33] W. Blendermann, Parameter identification of wind loads on ships, Journal of Wind Engineering and Industrial Aerodynamics 51 (3) (1994) 339–351.

[34] M. W. C. Oosterveld, P. van Oossanen, Further computer-analyzed data of the wageningen B-screw series, International Shipbuilding Progress 22 (251) (1975) 251–262.

[35] J. A. Taylor, Convex Optimization of Power Systems, Cambridge University Press, Cambridge, UK, 2015, see Sec. 4.1.2.

[36] A. Anvari-Moghaddam, T. Dragicevic, L. Meng, B. Sun, J. M. Guerrero, Optimal planning and operation management of a ship electrical power system with energy storage system, in: IECON 2016 - 42nd Annual Conference of the IEEE Industrial Electronics Society, 2016, pp. 2095–2099.

[37] MOSEK ApS, The MOSEK Optimizer API for Python Manual. Version 11.1 (2026). URL https://docs.mosek.com/11.1/pythonapi/index.html

[38] L.-P. Baillargeon, CVXship: Mixed-integer convex optimization for hybrid ship path planning and power management, https://github.com/LouisPhilippeBaillargeon/CVXship, GitHub repository, accessed July 13, 2026 (2026).

[39] Transport Canada, Protecting the North Atlantic right whale: Speed restriction measures in the Gulf of St. Lawrence—SSB No. 02/2026, https://tc.canada.ca/en/marine-transportation/marine-safety/ship-safety-bulletins/protecting-north-atlantic-right-whale-speed-restriction-measures-gulf-st-lawrence-ssb-no-02-2026, Ship Safety Bulletin, accessed July 11, 2026 (Apr. 2026).

[40] Copernicus Marine Service, Global ocean physics analysis and forecast, Product GLOBAL_ANALYSISFORECAST_PHY_001_024, dataset, accessed July 2026 (2026). URL https://data.marine.copernicus.eu/product/GLOBAL_ANALYSISFORECAST_PHY_001_024/description

[41] Copernicus Climate Change Service (C3S), ERA5 hourly data on single levels from 1940 to present, Copernicus Climate Change Service, Climate Data Store, dataset, accessed July 2026 (2018). URL https://cds.climate.copernicus.eu/datasets/reanalysis-era5-single-levels

[42] W. B. F. Ryan, S. M. Carbotte, J. O. Coplan, S. O'Hara, A. Melkonian, R. Arko, R. A. Weissel, V. Ferrini, A. Goodwillie, F. Nitsche, J. Bonczkowski, R. Zemsky, Global multi-resolution topography synthesis, Geochemistry, Geophysics, Geosystems 10 (3) (2009) Q03014, bathymetry accessed through the GMRT GridServer. URL https://www.gmrt.org/services/GridServer

[43] Hydro-Québec, Electricity rates, effective April 1, 2026, Rate D, Section 2. Accessed July 15, 2026 (Apr. 2026). URL https://www.hydroquebec.com/data/documents-donnees/pdf/electricity-rates.pdf

[44] Nova Scotia Power, Tariffs, https://www.nspower.ca/docs/default-source/regulatory/tariff-book-2026.pdf, schedule D, Shore Power Tariff, and Demand Side Management Cost Recovery Rider; accessed July 15, 2026 (May 2026).

[45] Grand Bahama Power Company, Equity rate adjustment, residential base rates effective with the June 2026 billing cycle. Accessed July 15, 2026 (2026). URL https://gb-power.com/era/

[46] Bahamas Power and Light Company Limited, Monthly fuel charge, fuel charge for February 2026. Accessed July 15, 2026 (2026). URL https://www.bplco.com/fuel-charge-update/

[47] Brunswick Electric Membership Corporation, Rate schedules, residential Service Schedule R, effective November 1, 2025. Accessed July 15, 2026 (Nov. 2025). URL https://www.bemc.org/wp-content/uploads/2025/11/BrunsRates_11012025_ncuc_approved-Final.pdf

[48] Bank of Canada, Daily exchange rates, daily average for July 15, 2026: 1 USD = 1.4049 CAD. Accessed July 15, 2026 (2026). URL https://www.bankofcanada.ca/rates/exchange/daily-exchange-rates/

[49] Central Bank of The Bahamas, About us, the Bahamian dollar is fixed at parity with the United States dollar. Accessed July 15, 2026 (2026). URL https://www.centralbankbahamas.com/about-us

[50] Y. Feng, O. el Moctar, T. E. Schellin, Parametric hull form optimization of containerships for minimum resistance in calm water and in waves, Journal of Marine Science and Application 20 (2021) 670–693.

[51] R. Vettor, J. Prpić-Oršić, C. Guedes Soares, Impact of wind loads on long-term fuel consumption and emissions in trans-oceanic shipping, Brodogradnja 69 (4) (2018) 15–28.

[52] M. Tadros, M. Ventura, C. Guedes Soares, Fuel consumption analysis of single and twin-screw propulsion systems of a bulk carrier, Journal of Marine Science and Application 22 (4) (2023) 741–750.

[53] Caterpillar Marine, M 25 E: 6-, 8-, and 9-Cylinder, Caterpillar Marine, efficiency and Performance—New Development; document LEDM0076-00 (Jun. 2014). URL https://www.teknoxgroup.com/fileadmin/user_upload/M_25_E.pdf